OPTICAL NANO-ANTENNAS: FABRICATION, CHARACTERIZATION AND APPLICATIONS

BY

ANIL KUMAR

DISSERTATION

Submitted in partial fulfillment of the requirements
for the degree of Doctor of Philosophy in Electrical and Computer Engineering
in the Graduate College of the
University of Illinois at Urbana-Champaign, 2011

Urbana, Illinois

Doctoral Committee:

Professor Jian-Ming Jin, Chair
Assistant Professor Nicholas X. Fang, Director of Research
Professor J. Gary Eden
Professor Brian T. Cunningham
Assistant Professor Xiuling Li

ABSTRACT

As optical counterpart of microwave antennas, optical nano-antennas are important devices for converting propagating radiation into confined/enhanced fields at nanoscale. The recent advances in resonant sub-wavelength optical antennas have now offered researchers a continuum of electromagnetic spectrum—from radio frequencies all the way up to X-rays—to design, analyze and predict new phenomena that were previously unknown. Their applications in areas with pressing needs, e.g., in sensing, imaging, energy harvesting, and disease cure and prevention, have brought revolutionary improvements. This dissertation investigates important characteristics of these plasmonic resonators through optical and electron-beam excitation using nanostructures defined by lithography as well as a newly developed direct metal patterning technique.

The important challenges in optical antenna research include both fundamental understanding of the underlying physics as well as issues related to fabrication of low cost, high throughput nanostructures beyond the diffraction limit. The nanoscale feature size of optical antennas limits our ability to design, manufacture, and characterize their resonant behavior. In this regard, I demonstrate how electron-beam lithography can be coupled with a new solid-state electrochemical process to directly pattern metal nanostructures with possibility of sub-10 nm features at low cost, minimal infrastructure, and ambient conditions.

Using bowtie antennas as representative of the general class of optical nano-antennas, I show how optical imaging can be used as a simple tool to characterize their resonant behavior. Further understanding of their spatial and spectral modes is gathered

using finite-difference time domain simulations. The extremely high fields generated in gaps of closely coupled bowties are used in non-linear signal generation and several sum-frequency phenomena are identified.

The sub-wavelength confinement of fields in optical antennas requires new techniques that can image beyond diffraction limited optical imaging. One such technique, cathodoluminescence (CL) imaging spectroscopy, which has been demonstrated to resolve sub-25 nm antenna modes, is used to map various modes of triangular and bowtie antennas. The highly localized electron-beam in CL is used to excite and map the hybridized modes of bowtie dimers, including anti-parallel "dark" modes. These high quality dark modes are critical for overcoming the fundamental limitations associated with wideband resonances in plasmonic resonators.

Finally, I discuss the role of CL in characterizing metal nano-disks which show multiple modes and have sizes comparable to their resonance wavelengths. CL provides a unique opportunity to map the enhanced fields from interference of surface plasmons sustained on the disks. The understanding of these modes is critical for the application of resonant metal cavities for the next generation of optical devices including nano-lasers.

To my family

ACKNOWLEDGMENTS

It is my great pleasure to thank everyone who has helped in making this work possible. First and foremost, I am sincerely thankful to my adviser, Prof. Nicholas Fang, for his guidance and support throughout my research. He has been an unending source of ideas and always took time to patiently discuss every detail of the work. His contagious enthusiasm and an open door policy for his students greatly helped in this work.

I am indebted to my academic adviser, Prof. Jian-Ming Jin, for agreeing to take the departmental responsibility for my thesis work. I would also like to thank Prof. Gary Eden, Prof. Brian Cunningham, and Prof. Xiuling Li for their valuable comments and the time they took to serve on my doctoral committee. I am also greatly thankful to Prof. Placid Ferreira and Prof. Kimani Toussaint for their guidance and the lively discussions during our meetings.

My colleagues have been a source of immense support during this work. I would specially like to thank Jun Xu, Kin Hung Fung, Keng Hsu, Pratik Chaturvedi, Chunguang Xu, Shu Zhang, Hyungjin Ma, Tarun Malik, Howon Lee, Kyle Jacobs, Bruno Azeredo, Kaspar Ko, Uttam Reddy, and Neville Dias for being part of the teams that helped solve numerous problems during this work. I am also thankful to Edmond Chow and Jim Mabon for trainings me; without their efforts this work will not be possible.

Finally, I would like to thank my family and many close friends. My wife, Mamta Singh, has shared the highs and lows of all these years. Her love and support helped me get past the worries throughout this work. Several close friends, including Kunal Srivastava and Jagannathan Rajagopalan added great memories during my stay in Champaign that I will always cherish.

CONTENTS

CHAPTER 1

INTRODUCTION

1.1 Background and motivation

Optical nano-antennas are the visible spectrum counterpart of microwave and radio frequency (RF) antennas [1-6]. The physics of these devices differs from RF antennas in two important aspects: first, due to high losses at optical frequencies, the assumption of perfect electrical conductor is no longer valid [7]; and second, due to unique phenomena at nanoscale, e.g., surface plasmon polaritons (SPP), the response of these structures can be quite different, the most notable of which is the subwavelength field confinement [3, 8]. Therefore, serious efforts are being devoted to extend current understanding from radio frequency antennas to their optical counterparts [5-6, 9-18].

Figure 1.1 makes a comparison between a radio frequency antenna and an optical nano-antenna. RF antennas with features of the order of several centimeters are important devices in modern communication. On the other hand, optical nano-antennas, with feature sizes of the order of a few hundred nanometers, find several important applications due to extremely high fields localized in subwavelength “hotspots” around them. Because of their small size, optical antennas offer several challenges including the capability to fabricate and characterize them. The high losses at optical frequencies pose another challenge and therefore limit the ability to extend current understanding from radio frequency antennas to the optical spectrum. Additionally, these new phenomena

require development of new modeling capabilities that can account for deviations from RF antennas to map their optical behavior.

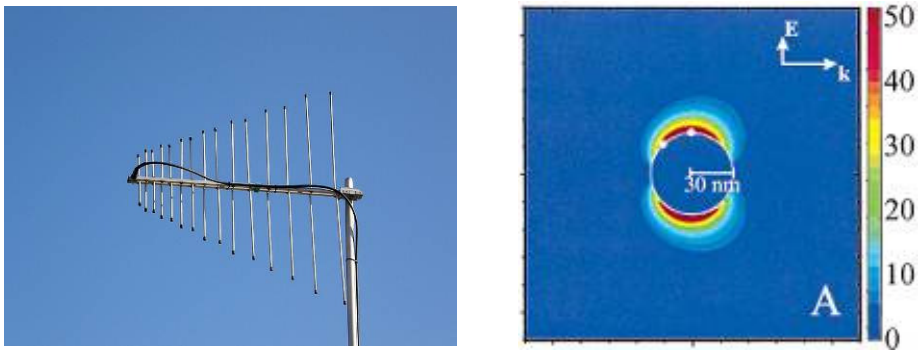

Figure 1.1: Examples of an RF antenna[1] (left, with characteristic dimensions of several centimeters) and an optical antenna (60 nm Ag nano-sphere resonant at 369 nm [18]).

This dissertation explores some of these challenges by taking new approaches in terms of fabrication as well as characterization. This section focuses on a review of important studies on optical nano-antennas. It includes recent observations reported for the general class of optical nano-antennas as well as findings unique to a triangular antenna and its dimer, the bowtie antenna. A wide range of applications of optical antennas have been reported in last decade and some of them are shown in Fig. 1.2. Clever techniques have been utilized for harnessing their rich physics for applications ranging from near-field light manipulation to single molecule sensing.

Optical nano-antennas have been used for several unique applications including cloaking [19], higher harmonic generation [20], biological and chemical sensing [21-24], sub-diffraction lithography [25], optical imaging [26], energy harvesting [27] and various other visible and near-infrared applications [28-30]. An important aspect of optical antennas is field enhancement in sub-wavelength regions that finds applications in

[1] Log periodic antenna for the VHS and UHF bands (140-470 MHz) ©2008 K. Krallis (www.wikipedia.com)

fluorescence and Raman spectroscopy with capabilities of single molecule sensing [21-24]. By placing dimers [31-35] or multiple particles [36-37] a few nanometers apart, unique phenomena can be observed, including dramatically high electromagnetic fields [33], polarization independent sensors [36], and color sorters [37].

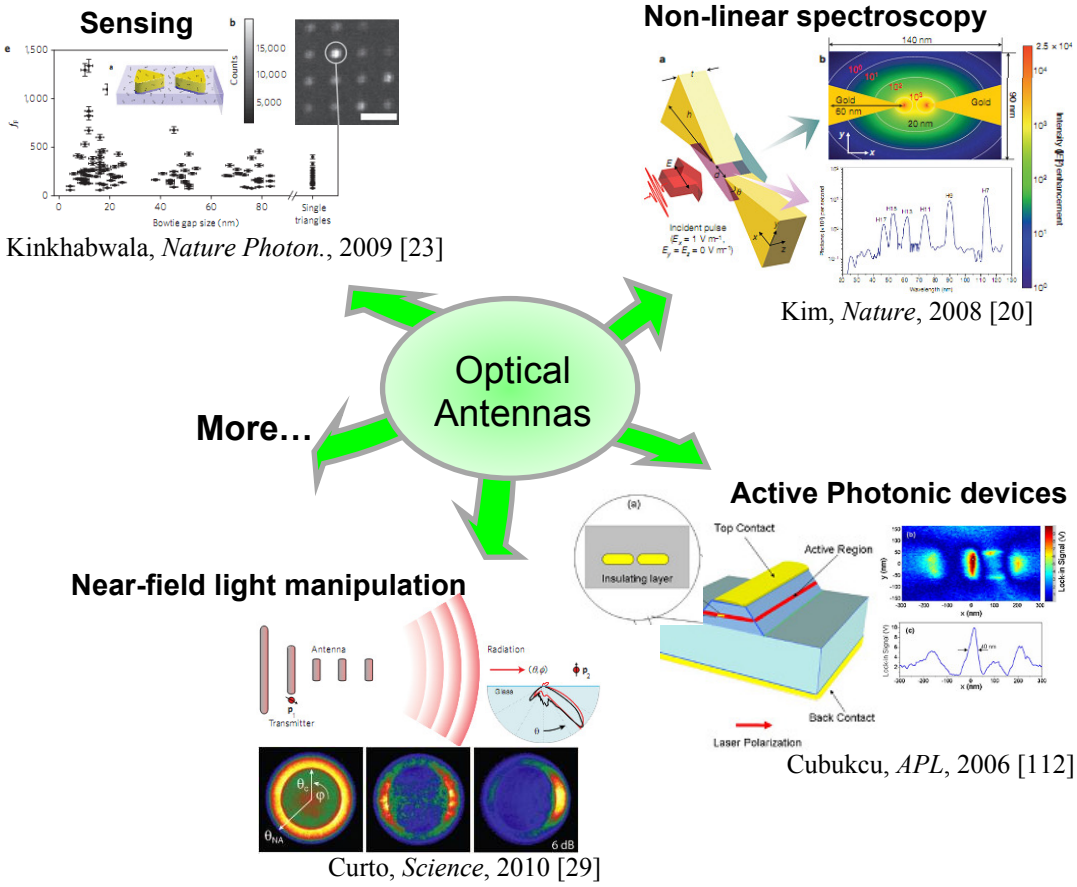

Figure 1.2: A wide range of applications are driving the current research in optical antennas. Some of the applications reported in recent years include biological and chemical sensing, non-linear spectroscopy and high-harmonic generation, photonic devices, high density optical data storage, sub-diffraction lithography and imaging, and solar energy harvesting.

A wide range of techniques have been utilized for characterizing the near-field as well as far-field behavior of optical antennas. Figure 1.3 lists some of these techniques

with a broad classification based on whether the input source and output detector is an electron or photon based system [38].

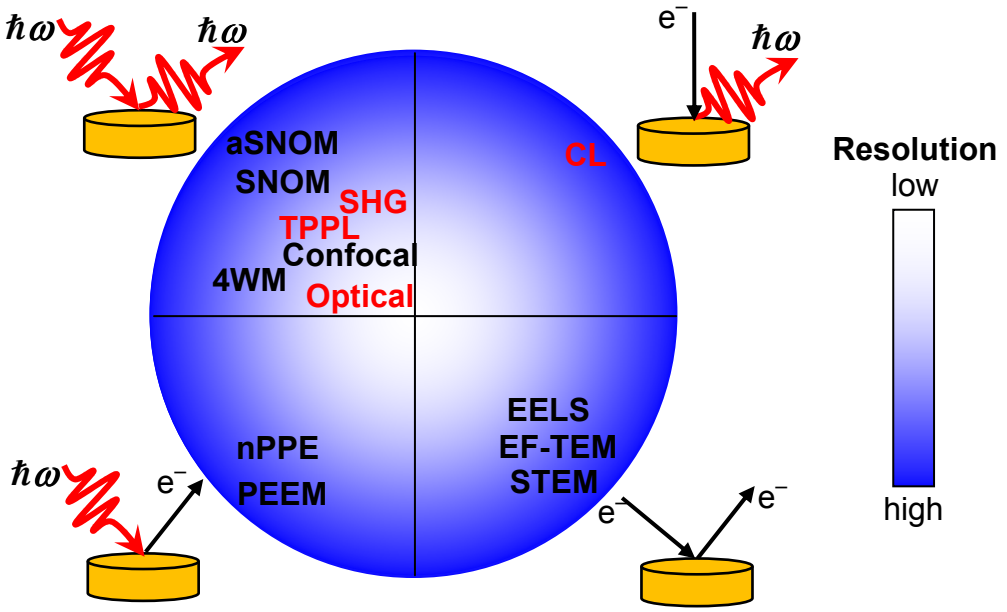

TPPL: two-photon photoluminescence	**4WM:** four-wave mixing
SNOM: scanning near-field optical microscopy	**SHG:** second-harmonic generation
aSNOM: apertureless SNOM	**nPPE:** n-photon photoemission
PEEM: photoemission electron microscopy	**EELS:** electron energy loss spectroscopy
TEM: transmission electron microscopy	**EF-TEM:** energy-filtered TEM
STEM: scanning TEM	**CL:** cathodoluminescence

Figure 1.3: Important techniques for real space imaging of optical nano-antennas [38]. The techniques are organized based on electron-photons as incident-emitted particles (and vice-versa) during characterization. Resolution limit increases from center to periphery. The techniques marked in red were used in this dissertation.

Photon-photon systems are the most widely used and have yielded the vast majority of the currently available information. Such optical measurements are the first and simplest approach for antenna studies [39]; however, their diffraction limited imaging prevents any spatial mapping of the resonant modes. Near-field scanning optical microscopy has been widely used for mapping the spatial information [40-41]; however,

the low signal and difficulty in performing experiments have forced researchers into developing new approaches of characterization. Non-linear processes [3, 30] including second-harmonic generation (SHG) and two-photon photoluminescence (TPPL) show better resolution than linear measurements, although the ability to generate these signals is still limited.

Electron-beam sources are another attractive approach for antenna studies due to the possibility of sub-Å resolution [42]. For this purpose, two techniques have recently become popular: electron energy loss spectroscopy (EELS) [42-43] and cathodoluminescence (CL) spectroscopy [42, 44-46]. The first technique, EELS, involves irradiation of the nanostructure with a highly accelerated electron-beam (~100 keV) and the subsequent energy loss to the resonant nanostructure is measured. This allows extremely high resolution with the ability to precisely control the location of excitation; however, the loss to optical antennas is only a few electron volts and requires strenuous efforts to resolve it, thereby limiting the spectral resolution. The second technique, CL, involves excitation using an electron-beam which perturbs the electron cloud in metal and the resulting plasmon oscillations emit photons that can be captured and characterized. Unlike EELS, where the sample needs to be electron transparent for mapping the losses in the electron-beam, CL can readily map surfaces as well as thick substrates. However, consideration needs to be given to signals generated from impurities as well as the effects arising from antenna substrates [46].

This dissertation focuses on some of the most important aspects of optical nano-antenna research. A broad approach is taken that involves fabrication as well as characterization using optical and electron excitation techniques. There are three main

objectives: (1) to design and fabricate nanostructures with the smallest possible features, at low cost, and good repeatability, (2) to understand their optical response and apply it to further extend that ability to new processes, e.g., in non-linear spectroscopy, and (3) to explore cathodoluminescence imaging spectroscopy as a unique technique to excite, map and understand various modes of the optical nano-antennas.

The first objective involves a broad exploration of nano-fabrication techniques that can help pattern metal nanostructures below 100 nm feature size with minimal complexity and good repeatability while using currently available tools. Out of several interesting geometries reported so far, triangular nanostructures were chosen. They are good candidates for current studies due to extremely high fields at their tips and predictable polarization dependence while maintaining minimal complexity. By placing another triangle nearby with controlled separation, a rich optical behavior can be designed. These bowtie dimers have been shown to generate extremely high fields in the gaps that are important for several applications. Because current electron-beam lithography technique can only fabricate gaps of up to 20 nm with good repeatability, further improvement in fabrication approach is necessary because the fields can be exponentially enhanced with further reduction in gap size [8]. A promising new approach is explored for this objective to generate sub-10 nm gaps in silver bowties [47-50].

The second objective involves exploring resonant behavior of the fabricated nanostructures using plane-wave excitation [39, 51]. The resonance behavior of optical antennas depends on several parameters including antenna size, underlying substrate, nature of input signal and interaction within an array. Beside exploration of some of these parameters, the nanostructures are investigated as possible candidates for new

applications, with one possibility discussed here being as a source of frequency multiplication [29]. The high fields in bowtie gaps are explored as a possible origin of non-linear phenomena including second-harmonic generation, two-photon photoluminescence and a new sum-frequency generation processes with below quadratic dependence [29].

In third objective, spectral and spatial mapping of various modes of optical nano-antennas using cathodoluminescence (CL) imaging spectroscopy [46] is explored. Most characterization techniques including near-field scanning optical microscopy (NSOM) and electron energy loss spectroscopy (EELS) suffer from low spatial or spectral resolution for mapping the near-field behavior. Scanning electron microscope based CL is ideally suited to map and resolve the "hotspots" of nano-antennas that are critical for a wide range of applications. The localized electron-beam in CL allows mapping of dark modes of optical antennas that cannot be readily excited with plane-wave sources [42, 51]. Additionally, larger nanostructures (e. g. nano-disks) showing multiple resonances can be easily studied allowing an unprecedented look at their optical behavior [52]. These studies extend the investigations of optical antennas into new class of optical devices, e.g., resonant metal cavities for enhanced spontaneous emission and lasing [53].

1.2 Thesis organization

In this dissertation, triangular nanostructures and their dimers (bowtie antenna), which can be used as a representative of the general class of optical nano-antennas, are studied, and some of the unique phenomena observed with these structures are explored. Chapter 1 provides a brief introduction, main objectives and organization of the thesis. In

Chapter 2, two approaches of fabricating the nanostructures are described. All the optical and CL characterization involved patterning using electron-beam lithography, and details of the design, fabrication, and possible modifications are discussed. Besides optimizing the e-beam lithography process, a new technique developed to fabricate large scale (up to several square millimeters) antenna arrays with sub-10 nm gaps is discussed. This technique, called Solid-State Superionic Stamping (S4), involves direct etching of metal films using a solid ionic stamp. In this work, S4 has been modified for fabricating the superionic stamps by embossing with Si templates. Various parameters of the microforming behavior are explored, and the role of deformation of the stamp, both at nanoscale as well as in bulk, is investigated. Additionally, new ways of improving the Ag film quality for patterning even smaller features are explored.

Chapter 3 describes optical characterization of nano-antennas using plane-wave excitation. The first part involves investigations of various parameters related to the linear response. Since arrays of antennas were studied, interference with nearby members resulted in near-field coupling and small peak shifts in extinction measurements. Details of this coupling and the effect of geometric arrangement on antenna response are described. In the second part, optical antennas as candidates for non-linear signal generation are explored. Besides second-harmonic (SHG) and two-photon photoluminescence (TPPL), a new non-linear signal with 1.7^{th} order dependence was observed. The strong dependence of linear antenna response on the non-linear signal was investigated using finite-domain time difference (FDTD) simulations.

Optical antennas can be characterized using several approaches involving plane-wave as well as electron-beam excitation. While Chapter 3 involved excitation using

plane-wave sources, Chapter 4 discusses characterization using an electron-beam source in cathodoluminescence imaging spectroscopy. Because the highly accelerated e-beam has wide range of momenta, it allows excitation of surface plasmons of all the possible wavelengths, which is especially important for high energy plasmons as well as for the dark modes not readily accessible with plane-waves. An electron-beam fixed near the antenna can excite completely different modes depending on its position, and several modes were identified for triangles as well as bowties. The effects of gap size and antenna loading were also investigated.

All the studies so far involved subwavelength resonant nanostructures. However, Chapter 5 discusses electron-beam excitation of nano-disks that are comparable in size to their resonant wavelengths. A strong dependence of beam location on excitation of different modes was observed. Depending on their size, several modes were identified. It was also observed that as the disk "circularity" changed from circular to square, broken degeneracy for a center-beam excitation revealed new modes. FDTD simulations using electron-beam source were used for further understanding of the nature of these modes.

Finally, Chapter 6 summarizes the findings and discusses the future outlook for optical nano-antennas. The field of optical resonators has immense potential and several new products involving optical nano-antennas are expected to reach the mainstream market in the very near future, including high-density data storage disks promised by Seagate [28]. In light of this progress, possible directions and new approaches for this ever expanding field are highlighted.

CHAPTER 2

OPTICAL NANO-ANTENNAS: DESIGN AND FABRICATION

2.1 Introduction

An optical nano-antenna is a noble metal nanostructure that can sustain electron-plasma oscillations leading to a resonant frequency that is proportional to its characteristic size **L**, and index of surrounding medium **n**. Similar to a microwave dipole, the resonant wavelength is given by $\boldsymbol{\lambda_{res}} = 2 \cdot \mathbf{n} \cdot \mathbf{L}$. Novotny [5] and others [6] have carried out rigorous calculations to derive a simple scaling law for gold nanorods to show that the resonant wavelength $\boldsymbol{\lambda_{res}}$ is dependent on type of metal (through λ_p, the plasmon frequency), antenna geometry, and the dielectric properties of the surrounding medium. Another way to "engineer" the antenna properties is by using a dimer antenna [54] and varying the gap between the particles [31-32, 34]. The dimers are strongly polarization dependent [3, 33], with a red-shifted peak for polarization along the dimer axis and a weak but slightly blue-shifted peak for normal polarization (Fig. 2.1).

The dimers are attractive because they allow enhancement of input signal (by $>10^3$) with extremely high intensities in the gaps [3, 33]. The high fields are important for several applications including sensing [21-24], high harmonic generation [20, 30], sub-diffraction lithography [25], imaging [19] and several other novel applications [19, 28-29, 36-37]. However, precise control over fabrication of the antenna gaps is critical for field enhancement [8, 14, 34, 37]. Current manufacturing techniques, e.g., electron-beam lithography, have the capability to fabricate sub-20 nm features; however, good control of

feature size as well as repeatability over large areas is essential for studying the antennas for possible applications. Additionally, the challenges of low throughput and high cost of the electron-beam lithography need to be addressed. Keeping these goals in mind, two different approaches for fabrication of the bowtie antennas were taken. In the first approach, electron-beam lithography was used to fabricate gold bowtie antennas with 20 nm gaps. In second approach, a novel technique recently developed in our group [47-50], called Solid-State Superionic Stamping (S4) was explored. The details of the modified S4 process to fabricate sub-10 nm features [49] with areas over several square millimeters [49-55] are explained.

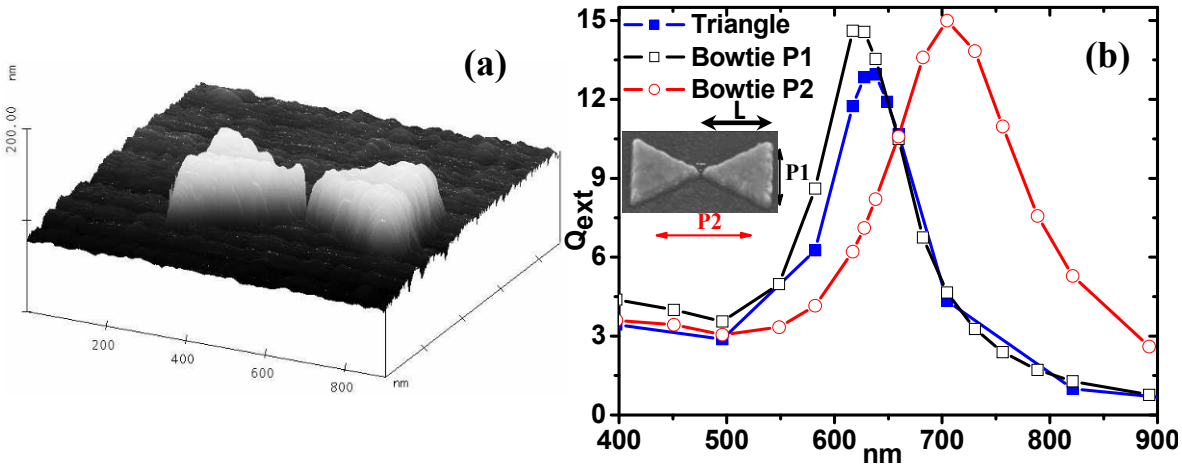

Figure 2.1: (a) Topographic image of a 120 nm Au bowtie antenna with 20 nm gap fabricated using electron-beam lithography; (b) DDA simulated extinction efficiency showing polarization dependence and splitting of triangle resonance mode into two orthogonal modes for the bowtie dimer (L = 120 nm).

2.2 Electron-beam lithography

Electron-beam lithography is one of the most common techniques to fabricate sub-100 nm features. Since this technique is highly matured and has been extensively used, only a general overview of fabrication steps is provided [49, 56]. For samples

fabricated for optical measurements, gold and silver nano-antennas were fabricated on 0.4 mm thick glass substrates with 25 nm thick ITO coating (CEC080P from Praezisions Glas & Optik GmbH, Germany). Samples for cathodoluminescence measurements were fabricated on 2 inch prime grade Si(100) substrates (from www.Universitywafers.com). The pre-cleaned substrates were first sonicated in an acetone bath for 5 min and dried at 200 °C for 2 min. Afterwards, Poly(methyl methacrylate) (PMMA) photoresist (2% solution of 95k mol. wt. in anisoline, from MicroChem Corp.) was spin deposited at 2000 RPM for 60 sec. The polymer was baked for 2 minutes at 200 °C resulting into ~ 90 nm thick resist layer. The e-beam lithography exposure was carried out at 20 nA beam current at various dose values. After exposure, the samples were developed for 180 sec in 3:1 solution of IPA:MIBK. All the silver samples were fabricated using e-beam evaporation (Cooke Evaporator) in the Micro and Nano Technology Lab at pressures below 8E-7 torr, with a 3 nm Cr adhesion layer underneath. The gold samples were fabricated with e-beam evaporators (Temescal) in the Materials Research Lab at pressures ~ 5E-6 torr, with 3 nm Ti adhesion layer. Finally, acetone was used for lift-off, followed by sonication in steps of 30 sec (but only when found necessary). Figure 2.1 shows images of bowties fabricated using this approach.

2.3 Solid-state superionic stamping (S4)

Hsu et al. [47-50] have previously reported a novel method of direct metal patterning using electrochemical etching with a superionic conductor “stamp.” An FIB-milled stamp was brought in contact with metal film and small external potential (~0.3 V)

and low pressure (< 10 MPa) were applied. Etching of the metal film at the contact region resulted in a metal pattern complimentary to the original stamp.

To effectively excite the nano-antennas, narrow gaps with precise control of the features are critical, with the ability to fabricate them over large areas. To overcome these constraints in S4, which is limited by the FIB-milling process, a new approach based on embossing was taken. The procedure and representative images during the various steps of the modified S4 are shown in Fig. 2.2.

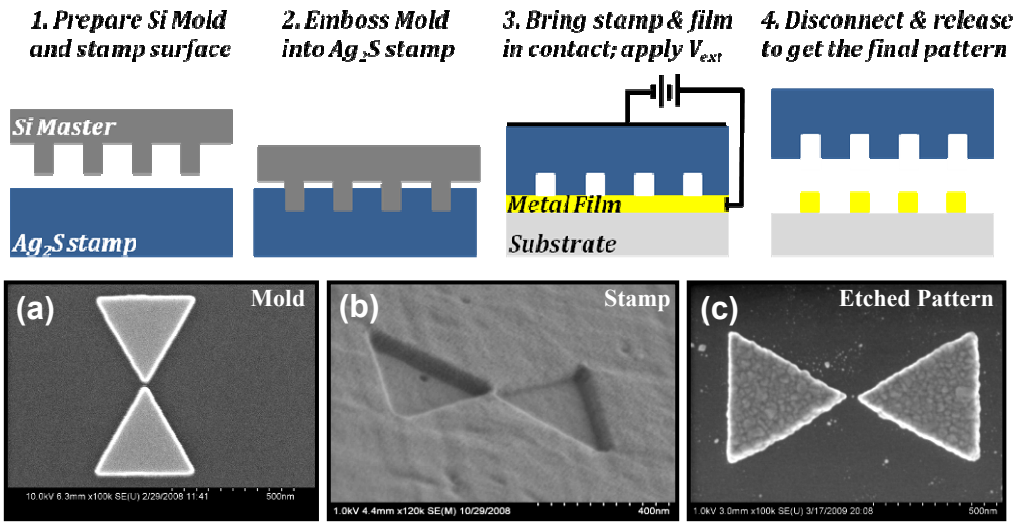

Figure 2.2: Various steps of the embossing based S4 process and representative images taken during these steps.

To summarize the process, Si molds were fabricated using e-beam lithography and reactive-ion etching (Step 1). This mold is then embossed into Ag_2S (Step 2) to generate a complimentary pattern, similar to the ones generated with FIB-milling. However, the S4 process can generate features beyond the capability of the FIB-milled stamps with appropriate modifications in the mold: e.g., side-wall cutting of the mold can be used for fabricating narrow lines and conformal alumina coating (using ALD) can be

used to fabricate very narrow bowtie gaps. Finally, the stamp fabricated using embossing is used for the direct metal etching of Ag film (Steps 3 and 4).

As shown in Fig. 2.3, gaps as small as 15 nm can be fabricated with yield greater than 25%. The smallest observed feature so far is about 8 nm [49]. The ability to use a Si mold for embossing into the superionic stamp suggests the possibility of patterning large areas. Figure 2.3 shows a linear grating fabricated over an area greater than 35 mm^2 as a proof of concept. Therefore, this approach has the potential to fabricate large arrays of antennas with very narrow gaps required for various applications of nano-antennas.

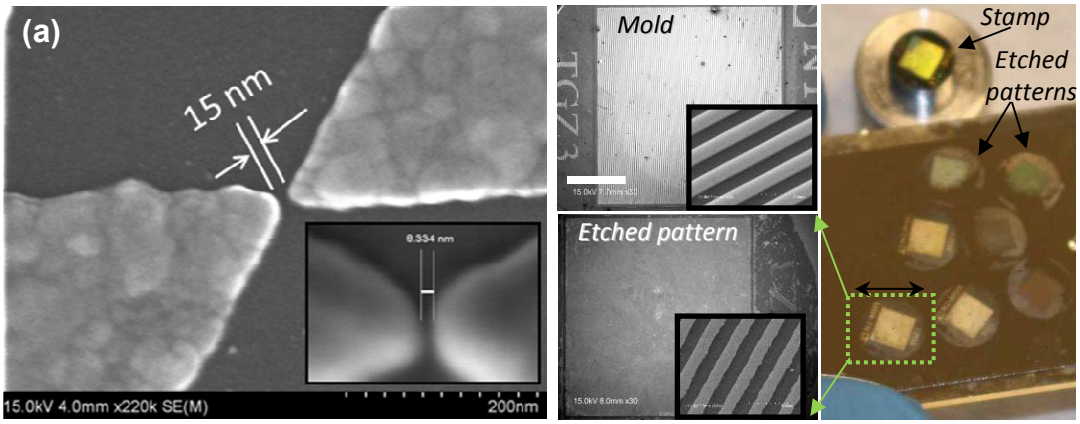

Figure 2.3: SEM images showing the capability of embossed based S4 approach for nano-antenna fabrication: (a) Gaps of 15 nm with high reproducibility (and smallest reported gap of sub-10 nm); (b) a proof of concept images showing large area patterning of a linear grating.

2.4 Role of mechanical deformation in stamping

The silver patterns fabricated using embossing based S4 process involve mechanical deformation of the ionic conductor. Not only does such a deformation affect the final features, but a strong modification in the ionic properties of the stamp is observed. Understanding the role of local as well as bulk deformation on the mechanical and ionic properties of Ag_2S is important for understanding the capabilities of this

approach. Additionally, it allows extending this process beyond the current fabrication methods, which can be important for future work involving S4 process.

2.4.1 Nanoindentation

An important characteristic of silver sulfide (Ag_2S) is its favorable mechanical properties for microforming [49, 57]. Unlike most ionic conductors, Ag_2S is ductile and has relatively low yield strength of 80 MPa. To explore the embossing behavior of Ag_2S stamps, nano-indentation is used, which is a common method to measure mechanical properties of small volumes, thin films and interfaces. Figure 2.4 shows measurements on a microtomed Ag_2S surface under different loading conditions. A reduced Young's modulus of 30 GPa and hardness of 0.6 GPa are observed.

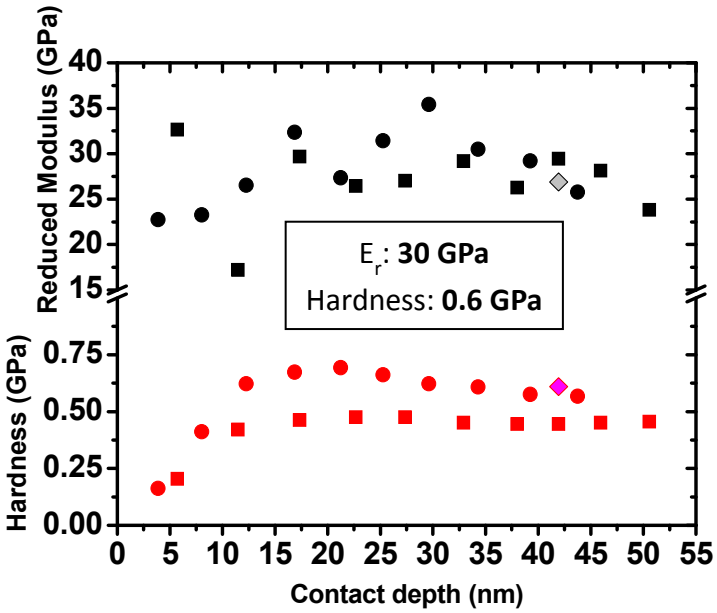

Figure 2.4: Modulus and hardness of Ag_2S measured using single-step (diamond) and multi-step (square & circle) nano-indentation of stamp surface.

These values are comparable to the corresponding values for softer metals, e.g., Sn and Au. The elastic modulus is about four orders of magnitude higher than PDMS

(and about 10 times higher than PMMA), and the hardness is about two orders higher than PDMS [49], suggesting that some of the common issues related to stamp collapse [58] are highly improbable for Ag_2S. This comparison also gives an idea of the stress required for embossing Ag_2S: the modulus is sufficiently high to form patterns with well-defined features, but relatively low enough to not require serious investment in embossing equipment.

2.4.2. Bulk deformation and etch rate enhancement

To understand the effect of forming procedures, one needs to understand the electrochemical processes and effect of bulk deformation on them [57]. Since Ag_2S is a mixed conductor, complex electrochemical changes for both electrons as well as ions are observed [59-60]. Incorporation of Ag into β-Ag_2S—which is the room temperature phase used in the experiments here—can be modified by applying external pressure on the stamp. For mixed conductors, the electronic current is mostly parasitic and it is always desirable to achieve as high an ionic current as possible. By deforming the polycrystalline conductor electronic current is reduced while total current density of the system is enhanced [57]. Besides quicker etching, such an enhancement has applications in faster charging of batteries and ionic actuation.

For characterizing bulk deformation, Ag_2S crystals grown in-house [47-48] were tapered into conical tips and a mesa of about 500 μm was formed by microtoming the tips. Such a mesa was pressed against a Si wafer under constant load to flatten the surface and get an approximately similar mesa diameter at every step. Afterwards, this surface was brought in contact with an amorphous Ag film and on application of an external

potential of 0.4 V, etching of silver films was observed. Etches were randomly performed for different time intervals without etching all the way through the film. Before and after these etches (lasting about 30 minutes), a 50 nm gold film was used to measure the electronic current for a few seconds. Once these steps were completed, the conical part of the crystal (~0.5 mm length) was cut off to eliminate the tip with excess silver transported into the crystal. A closed die was used to press this crystal to a load of four times the yield strength of the Ag_2S (~80 MPa) as shown in the schematics of Fig. 2.5 (a). Afterwards a conical tip of the same size and angle was formed to repeat the etching process as earlier. These steps were repeated for several deformation stages of the same crystal to study the effect of deformation on the transport properties of Ag_2S.

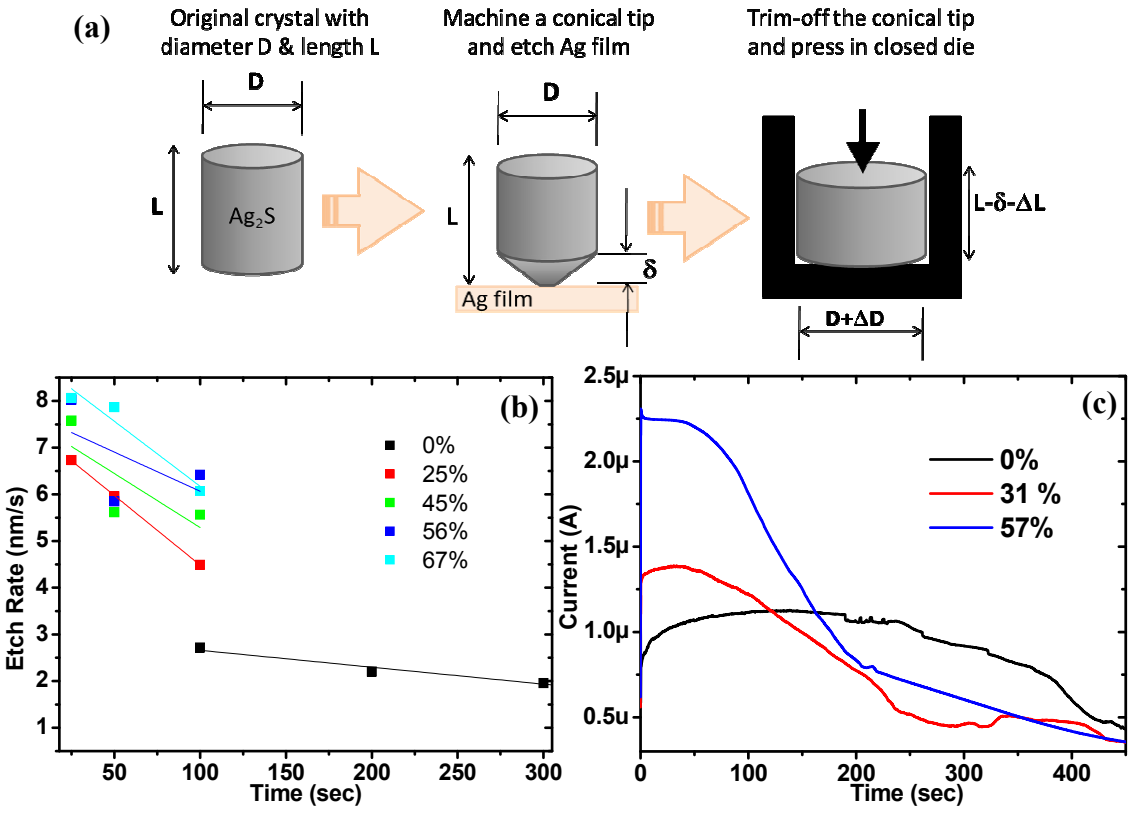

Figure 2.5: Steps involved in bulk deformation of Ag_2S (a) and its effect on the Ag film etch rate (b) and the corresponding current density measured during etching process (c).

To understand the effect of deformation on metal dissolution, partial etching of silver film at various stages of deformations was performed. Figure 2.5 (b) shows etch depths of an amorphous Ag film at various time steps measured using atomic force microscope (AFM) scans. It can be clearly seen that the deformed crystals required shorter time intervals to dissolve similar thicknesses compared to the original crystal. As an example, a crystal deformed to 67% of original length required only one-third the time taken by the original crystal to dissolve the same depth of silver film, therefore resulting into three-fold etch rate enhancement. The current density also increased with several interesting features observed in the temporal profile of the current passing through the interface. Figure 2.5 (c) shows enhancement of the current density at the start of etching which dips sharply over time. For undeformed crystal, the current saturates, suggesting transport to be a limiting factor; however, deformation increases the dislocation density and this barrier is modified. Further analysis of the electronic current against a gold film showed reduction in electronic current attributed to scattering of electrons by dislocations. This drop also suggests an overall increase in the ionic current resulting in modification in the energy barrier to oxidize and transport silver across the interface.

2.5 Improving silver film quality

Silver is currently the most important plasmonic material for optical devices including optical antennas. Due to its lower bulk electrical resistivity (1.57 $\mu\Omega$cm at room temperature) and resistance to electromigration in metal interconnects, silver is also a potential material for achieving higher current densities and faster switching speeds. Despite several decades of efforts, there exists a lack of control over film growth of silver

films, due to its high mobility and island-like growth. Therefore, improving device performance by growing high quality films is of enormous interest. A new approach of improving the Ag film roughness by depositing a very thin Ge buffer layer has been shown earlier, which changes the thermodynamics of film growth [61]. Here, a new approach using MgO buffer layer, which has very small lattice mismatch with Ag, is used that allows epitaxial growth of very thin metal films with extremely low roughness.

Besides metal films, metal-oxide structures are important in several applications including metal-oxide-semiconductor field-effect transistors (MOS-FET), magnetic tunneling junctions (in magnetoelectronics and magnetic data storage), and in oxide heterostructures, as well as in catalysts, corrosion resistance coatings and sensors. MgO is specifically suited due to the large band-gap of 7.8 eV [62]; it has been shown that epitaxially grown MgO films as thin as three monolayers can maintain a high band gap of up to 6 eV [63]. Additionally, MgO has low dielectric constant (n=1.7), low optical loss, excellent high-temperature chemical stability as well as excellent thermal conductance. The Ag-MgO system is specifically interesting due to very low lattice mismatch (<3%) [64], which is expected to result in reduced defects and more uniform films. Therefore, Ag films grown on MgO should offer improved film quality as well as a better metal-dielectric combination. However, low lattice mismatch is no guarantee for smooth films since silver films on MgO (or in general metal films on oxides) grow by Volmer-Weber mode (i.e., island-like growth) [65]. This is a serious concern for silver films due to the very high mobility of adsorbed Ag adatoms. The important drawbacks of this are higher losses in optical nanostructures and enhanced resistivity due to scattering in electronic devices. Besides these limitations, the quality of both the MgO and MgO/Ag films can be

dramatically improved by using a very thin (0.1-1 nm) silver layer on top of the Si/SiO_2 substrate. This is confirmed using morphological studies of the films using AFM, and large area uniformity of the films using X-ray reflectivity. Since electronic devices are susceptible to temperature fluctuations, effect of annealing on the MgO/Ag films is also studied.

2.5.1. Film growth and characterization

Silver and MgO films were deposited using electron-beam evaporation at a rate of 0.5 Å/s and base pressure of $5x10^{-6}$ Torr. MgO was purchased from Kurt J. Lesker as fused pieces (99.95% purity) and was evaporated without any oxygen atmosphere. Prior to deposition, the Si(100) substrates (from www.Universitywafer.com) were cleaned using acetone, deionized water, and ethyl-alcohol, and blow-dried using nitrogen. No additional cleaning or removal of the native oxide was performed.

AFM measurements were performed on a Digital Instruments/ Veeco Dimension 3100 atomic force microscope with standard tips. The X-ray reflectivity measurements were carried out using a state-of-the-art modular 'Xpert' XRD system (from Philips) mounted with Cu X-ray source. A slit width of 1 mm was used for all the measurements. For resistivity measurements at elevated temperatures, annealing of the films was carried out in an RTP setup (from ULVAC) with a base pressure of 7E-7 Torr and a rise time of 3 minutes to reach the maximum temperature.

AFM

Due to the small lattice mismatch between silver (d = 4.09 Å) and MgO (d = 4.21 Å) [64] minimal strain is expected as the top layer grows. However, several parameters

affect the film growth, and lattice mismatch alone may not guarantee better film quality. In general, direct growth on Si without a native oxide layer is usually not possible and a thin oxide layer forms during sample loading and pump-down even on HF cleaned substrates [66]. From Ag growth perspective, the presence of the oxide layer has no significance since the substrate will only affect the initial mismatched MgO growth of a few monolayers [67]. To understand the behavior of MgO film growth, several different thicknesses were deposited to understand the MgO film quality on Si/SiO_2 substrate. AFM scans of 3 to 15 nm MgO films show that the thicker films tend to have larger grains with a peak-to-valley size changing from 2.32 nm (3 nm MgO) to 4.59 nm (15 nm MgO). Similarly, the roughness increases from 0.42 nm to 1.41 nm. When silver is deposited on top of these films, they further increase the film roughness as shown in AFM scans of Fig. 2.6 for a 15 nm Ag film on 15 nm MgO layer. The granular films with high pin-hole density have roughness of 5.01 nm and peak-to-valley difference of about

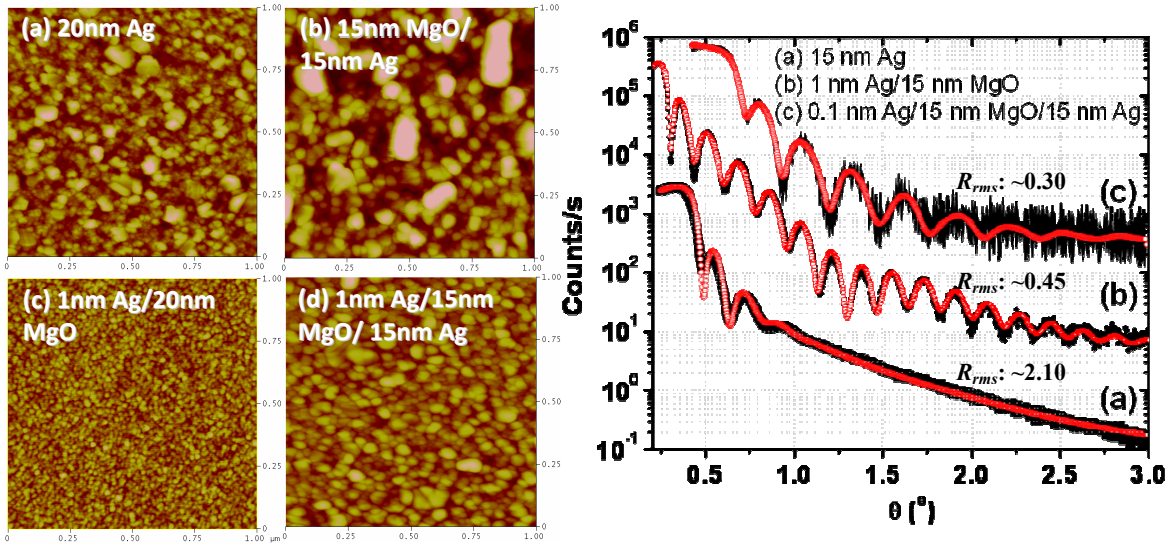

Figure 2.6: Improving Ag thin film quality using MgO buffer layer. (Left) small area AFM scans with different topography dependent on the MgO buffer layer. (Right) X-ray reflectivity measurements indicating long range order in the films.

22.20 nm. These values are almost double that observed for a 15 nm Ag film directly deposited onto Si/SiO_2 substrate.

Introduction of a very thin Ag layer (0.1-1 nm) underneath the MgO layer dramatically changes the film properties. As seen in the surface scans of Fig. 2.6, a 20 nm MgO film on 1 nm Ag layer shows very small particle size (peak-to-valley size of 1.62) and an almost six-fold improvement in the film roughness (0.30 nm), thereby making these films more dense and smoother than the original films. When a 15 nm silver film is deposited on such an Ag/MgO multilayer structure, the overall properties of the silver films improve and are confirmed with XRR measurements. To understand the role of the thin Ag layer underneath MgO, 0.5 nm Ag film on Si/SiO_2 substrate was deposited. Due to high mobility and island-like growth of Ag, a discontinuous film with islands as tall as 8-10 nm and particle diameter in the range of 10-50 nm was observed. Therefore, MgO films grown on this base layer have an interface that is a combination of Ag and SiO_2, which seems to provide large nucleation sites and inhibition of particle growth.

XRR

X-ray reflectivity measurements were carried out on samples with areas larger than 1 cm^2. A 20 nm MgO layer with a 1 nm base layer of Ag on Si/SiO_2 shown in Fig. 2.6 was used for the XRR measurements. The large number of fringes appearing in these scans show a high degree of ordering observed in the films. The roughness values observed from the fitted curves is about 0.4 nm. When a similar multilayer structure with 15 nm MgO and 15 nm Ag top layers was measured, it showed several interference fringes and roughness as small as 0.45 nm, compared to a similar multilayer structure but without the thin Ag layer underneath the MgO. In comparison, a 20 nm Ag film directly

deposited onto Si/SiO_2 substrate shows roughness of about 2.2 nm and has been reported to be significantly rougher [61].

2.5.2. Effect of annealing on film resistivity

One of the most important aspects of metal-interconnect studies is film quality at elevated temperature. It has been found that film resistivity increases at higher temperature due to enhanced scattering. One important aspect is to study the effect of annealing temperature on the film continuity, and for that matter, the resistivity of the films. In general, temperature and time have similar effect; the films will eventually granulate if kept at low temperature for long time or at high temperature for short period of time. Since the MgO-Ag bonding is physisorption, with bond energy of 0.3 eV/atom [68], the films will eventually granulate.

To investigate the effect of the elevated temperature, we annealed (under pressure of 7E-7 Torr) 10 nm and 15 nm Ag films on 15 nm MgO (with 1 nm Ag base layer on Si/SiO_2) layer. As a general trend, for annealing at 100 °C, no appreciable change in resistivity was observed for annealing time >5 hours. However, for annealing at 150 °C, the resistivity slightly increased as shown in Fig. 2.7 and the films were continuous for about the first 3.5 hours of annealing. At 200 °C, the films granulated within an hour of annealing. For the results shown in Fig. 2.7, all the films were deposited on Si/SiO_2 with a thin 0.5 nm Ag layer below the MgO film (as this Ag layer was observed to improve the smoothness). 15 nm Ag film on 15 nm MgO annealed at 100 °C shows small increase in resistivity and was found to be continuous even after 5 hours of annealing. Films annealed at 150 °C became discontinuous after 3.5 hours of annealing. For higher temperature, e.g., at 200 °C the films were no longer continuous even after 1 hour of

annealing. Note that films grown on 6 nm MgO films show resistivity close to the bulk silver resistivity (1.57 uW-cm). Also, a 10 nm thin film on 15 nm MgO shows relatively low resistivity of about 10 times the bulk resistivity. Therefore, as a general rule, temperature seems much more important parameter than duration of annealing. Most of the resistivity increase is within one order of magnitude, until the films became discontinuous, which seems to happen rather dramatically beyond a certain annealing time.

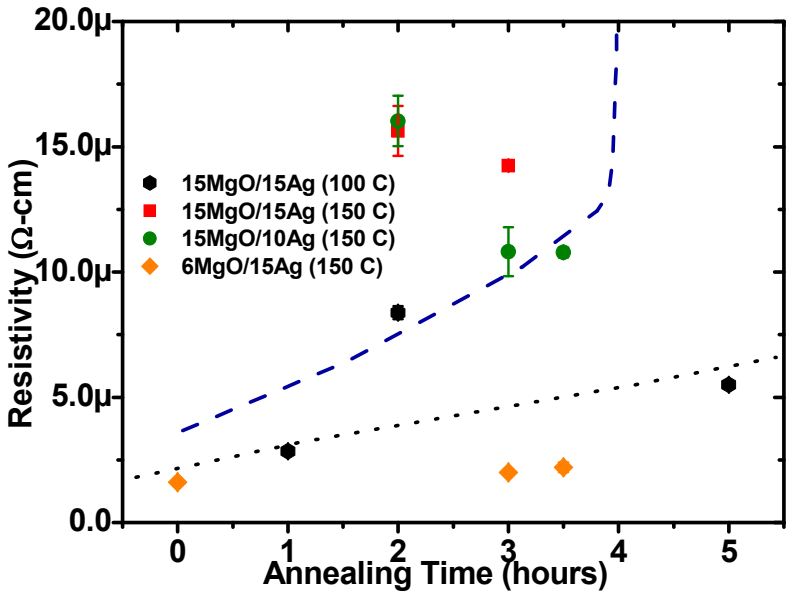

Figure 2.7: Effect of annealing on Ag films deposited on 0.5nm Ag/15 nm MgO and Si/SiO_2 substrates. Once the films become discontinuous the resistivity jumps dramatically as shown for the 15 nm MgO/10 nm Ag film annealed at 150 °C.

2.6 Summary

Two different approaches of optical nano-antenna fabrication are discussed. The first approach involved samples fabricated using electron-beam lithography with bowtie gaps as small as 20 nm. These samples are used for characterization throughout this

dissertation. The second approach discusses a method based on a newly developed technique called Solid-State Superionic Stamping (S4), which is a low cost and high throughput alternative to the electron-beam fabrication. In this process, a solid ionic conductor stamp of Ag_2S was first embossed with a Si template and subsequently used to etch Ag films under ambient conditions, low pressure, and small external potential. Sub-10 nm gaps in bowtie antennas with the capability to fabricate nanostructures over several millimeters were demonstrated. Mechanical deformation of stamp and quality of silver films have significant effect on the S4 process Therefore local as well as bulk deformation of Ag_2S stamp was investigated. A new approach of film growth based on MgO buffer layer for Ag films demonstrated sub-nm film roughness.

CHAPTER 3

OPTICAL CHARACTERIZATION OF NANO-ANTENNAS

3.1 Introduction

The collective oscillation of electrons in noble metal nanostructures, called localized surface plasmon polaritons (SPPs), are characterized by strong interaction of the conduction electrons with incident radiation. This interaction, at their resonance frequency, results in strong scattering, absorption and local field enhancement near the nanostructures. The process of scattering and absorption involves slow dephasing of the optical polarization associated with the electron oscillation [69-70]. Consequently, the decay of the plasmons into photons occurs either through emission of photons (radiative process) or loss to electron-hole excitation (non-radiative process). Reducing the non-radiative losses means emission of photons can be maximized and the highest field enhancement can be achieved with the optical polarization. When measured using standard optical spectroscopy, these processes result in a dip in the transmission spectrum [39] and a strong near-field enhancement around the nanostructures [3, 33]. Most efforts are therefore focused on understanding the behavior of a given system through optical measurements complemented with simulations. Once characterized, this approach allows application of the localized SPPs in a wide range of applications including surface-enhanced Raman spectroscopy [24, 71] and non-linear spectroscopy [3, 20, 30]. The enhanced fields are specifically important for processes involving sum frequency generation since the resulting high photon densities increase the probability of photon combination [20, 30]. Therefore, optical characterization is the first step in understanding

the nature of particle resonance, near-field distribution and possible applications in various areas including non-linear spectroscopy.

In this chapter, important parameters of optical antennas are discussed using electron-beam fabricated Au bowtie nanostructures [39, 56]. Far-field transmission measurements were used to derive scaling laws confirming antenna resonance as a linear function of nanostructure size. For high signal-to-noise ratio, the measurements were performed on large arrays of bowties. The antenna array spacing is therefore an important parameter for these studies. Closely spaced arrays show stronger interaction and blue-shift in resonance peaks. Both experimental as well as simulated results using finite-difference time-domain (FDTD) and Discrete Dipole Approximation (DDA) [72] are considered. Based on understanding of linear response, experiments were carried out to study the non-linear response of arrays with different antenna spacing. Beside second-harmonic generation (SHG) and two-photon photoluminescence (TPPL), a new non-linear process with sub-quadratic response was observed. Finally, efforts on using the linear response to understand and predict the non-linear response are discussed.

3.2 Linear response and array effect

3.2.1 Antenna extinction cross section

For any optical studies, the first step in characterization of antennas involves excitation of the nanostructures using a broadband source. The transmitted signal shows a dip in the spectrum corresponding to the antenna resonance. At this wavelength, the incoming radiation has the highest coupling with the structures. To quantify the quality of

this interaction, the most common method is to measure the scattering cross section [4, 73], which is related to the ability of the antenna to scatter, absorb and reradiate the incoming radiation. A large cross section means high interaction volume of the nanostructure, providing better sensitivity to the nearby molecules and other species used for sensing. During optical measurements (inset, Fig. 3.1), the transmitted intensity $\boldsymbol{I}$ at the spectrometer is a function of the incident beam power, and absorption and scattering by the antenna at each wavelength, which can be expressed as [4, 39, 73]

$$\boldsymbol{I}(\lambda) = \boldsymbol{I}_{inc}(\lambda) - \boldsymbol{I}_{abs}(\lambda) - \boldsymbol{I}_{s}(\lambda),$$

where $\boldsymbol{I}_{inc}$ is the intensity of the incident beam (the intensity measured without samples), $\boldsymbol{I}_{abs}$ is the intensity loss due to absorption in the antenna, and $\boldsymbol{I}_{s}$ is the intensity loss due to scattering in all directions.

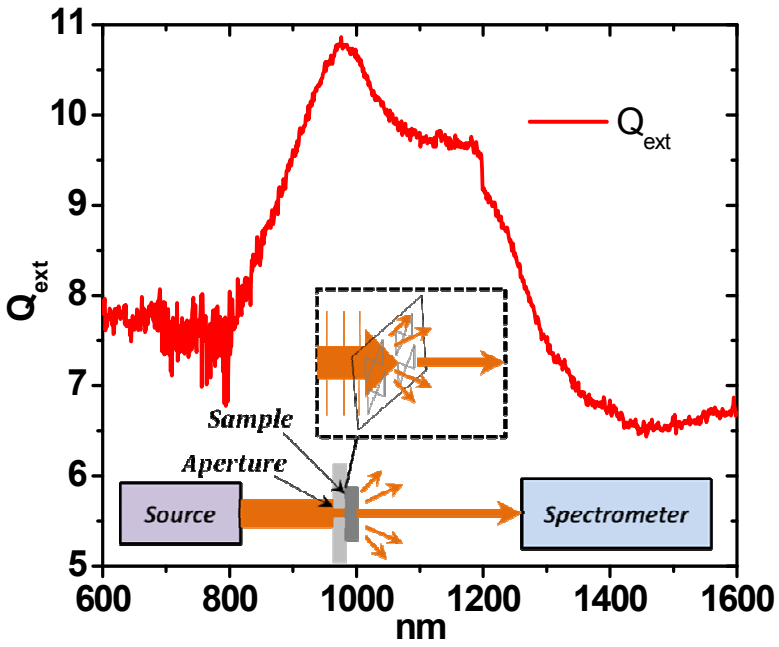

Figure 3.1: Extinction efficiency of a 240 nm bowtie array spaced 3 μm apart. Inset shows sketch of the measurement setup. A resonance peak at 960 nm is observed (the peak at 1200 nm is due to change in detector in measurement setup).

Also, the transmitted intensity can be written as

$$\boldsymbol{I}(\lambda) = \boldsymbol{I}_{inc}(\lambda) - \boldsymbol{C}_{ext} \times \boldsymbol{S}_{inc},$$

where $\boldsymbol{S}_{inc}$ is the power density at the sample and $\boldsymbol{C}_{ext}$ is extinction cross section of the antenna. $\boldsymbol{C}_{ext}$ can also be regarded as the area of "geometric shadow" of the antenna, since the rate at which energy would impinge upon this area equals the actual rate of energy removal from the incident beam due to scattering and absorption by the antenna. From this measurement, extinction efficiency can be derived, which is extinction cross section divided by actual geometric cross section of the nanostructure.

Figure 3.1 shows the extinction efficiency, Q_{ext}, of a 240 nm bowtie antenna measured for arrays that are spaced 3 μm apart in both directions for minimal interaction. At resonance peak of 960 nm, highest efficiency, Q_{ext} ~11 was observed, indicating that on the spectrometer, the antenna appears almost 11 times larger than its geometrical size. This high extinction value for the lithographically designed nanostructures suggests excellent uniformity in fabrication as well as in the ability to efficiently excite them.

3.2.2 Antenna scaling laws

For designing antennas with appropriate resonance wavelengths, experiments were performed on lithographically fabricated nanostructures with various sizes. Figure 3.2 (a) relates the resonant wavelength with triangle length (tip-to-opposite edge) of bowties and the substrate index, $\lambda_{res} = 2 \cdot n \cdot L$. The actual system is more complex due to the presence of 25 nm ITO (n=1.95) and the coupling between the triangles. However, the observed slope is comparable to RF dipoles, suggesting this simple relationship holds for these nanostructures at near-IR wavelength range, as suggested earlier [5-6].

3.2.3 Polarization dependence

Triangular structures are polarization independent [74]; however, bowties show a strong dependence on polarization of the applied field. The two main polarizations, along bowtie axis and normal to axis, will excite different modes (Fig. 3.2 (a), also see Fig. 2.1). Polarization along the long axis will result in strong interaction between the two triangles leading to a stronger and red-shifted peak. This polarization also results in very high fields in the gap due to strong charge interactions at the tips of the triangles [25, 33-34]. However, for normal polarization the tips at the gap have minimal contribution to charge oscillations resulting in resonance behavior similar to two independent triangles.

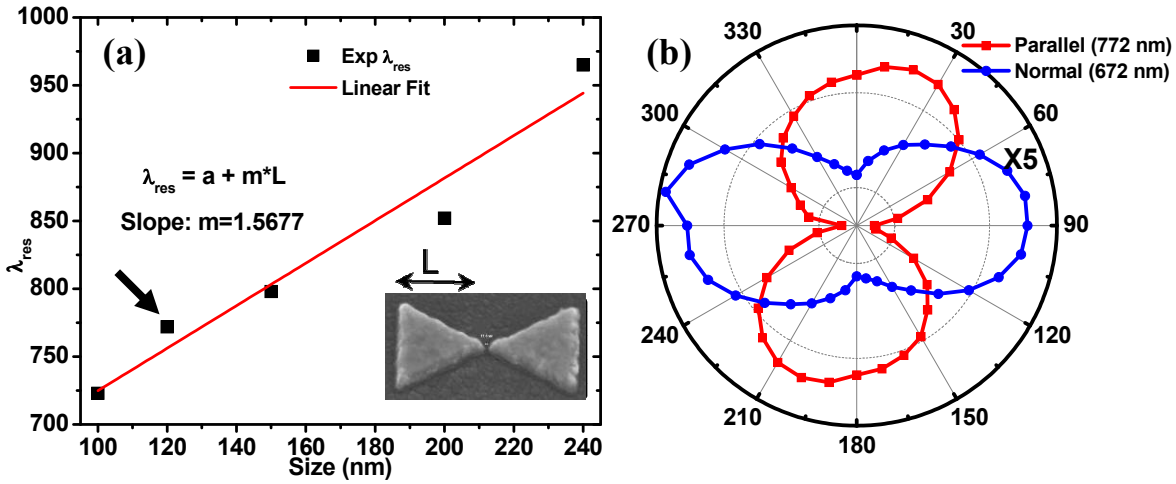

Figure 3.2: Characterization of bowtie antennas using optical excitation. (a) Measured extinction peaks as a function of triangle size for various bowties with 20 nm gaps. (b) Polarization behavior of a 120 nm bowtie antenna (marked with arrow). Polar plots are shown for the two orthogonal bowtie modes (the weaker mode is enlarged five times).

3.2.4 Field enhancement

Simulations of near-field provide insight into the enhanced fields in the gap that are important for chemical and biological sensing [21-24]. Figure 3.3 (a) shows the near-

field of a bowtie plotted 2 nm above Au surface using DDA [72]. Complementary experimental results are used to confirm the predicted high fields. Figure 3.3 (b) shows an SEM image of bowties taken after excitation using a high power laser with tightly focused beam spot (more information on the experiment is provided in Section 3.3). When excited near resonance (at 780 nm), enhancement in the intensity in the gaps of the bowties should be observed. Beyond a certain threshold power (>23 mW), the field enhancement will be large enough to modify the nanostructure and the first signs of damage should start appearing in the gap. The two damaged bowties in Fig. 3.3 (b) confirm this hypothesis, and the damage profile in the gaps matches with simulated high fields.

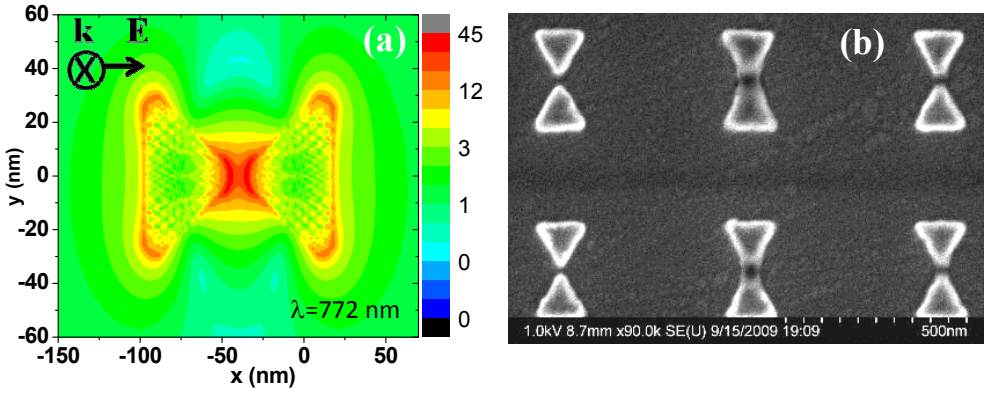

Figure 3.3: (a) DDA simulated near field of a bowtie antenna; (b) melting of the bowtie tips observed after excitation using a pulsed laser at 780 nm and 23 mW input power.

3.2.5 Antenna arrays

Optical antennas are seldom probed individually due to low signal-to-noise ratio. However, the array behavior of antennas can be dramatically different from that of individual nanostructures due to strong interactions [75-76]. When considering ordered

arrays of nanoparticles, the polarizability of nanoparticles in an array also involves their geometric arrangement factor, *S*, and is given by [77]

$$\alpha^* = \frac{1}{1/\alpha - S}$$

where α is polarizability of a single particle. From this expression, when the two terms in denominator are comparable, particle polarizability in arrays can be enhanced, resulting in resonances that are strongly influenced by the spacing in arrays. Examples of such a modification of resonance behavior are shown in Fig. 3.4. As the particles are brought closer, the dominant mode shows sharper resonance [76] as well as significant blue-shift (inset Fig. 3.4 (a)). This behavior is confirmed through FDTD simulations of various spacing in Fig. 3.4 (b). Therefore, any studies involving arrays of nanostructures need to account for the significant shift in resonance peaks based on their arrangement.

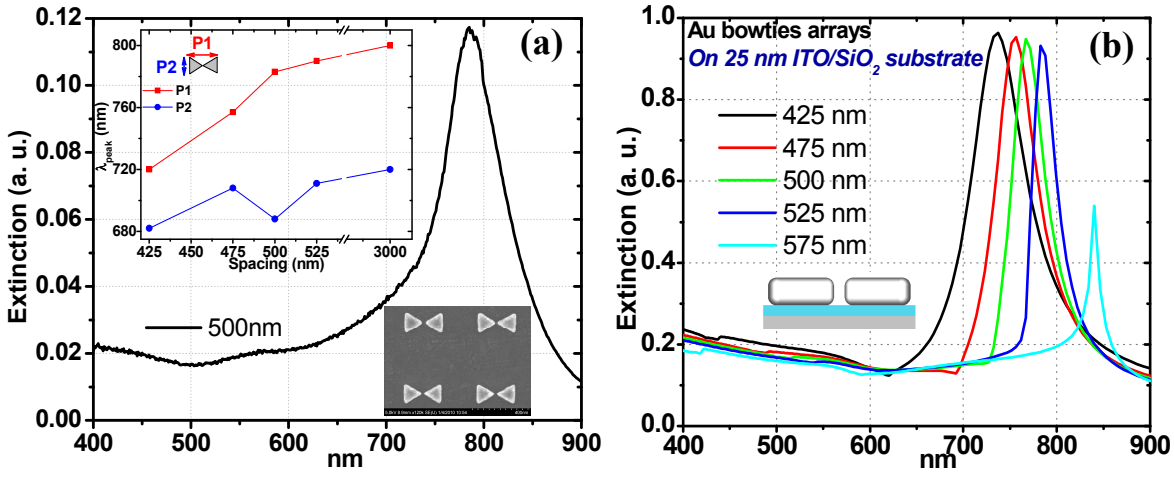

Figure 3.4: Array behavior of bowtie antennas. (a) Experimental extinction measurement of an array of 120 nm bowties with 500 nm spacing. Inset shows shift in peak wavelength for the two modes as a function of array spacing; (b) FDTD simulations confirming the experimental observations.

3.3 Optical antennas for non-linear spectroscopy

Sum frequency generation processes are dependent on several factors, including local photon density, which can be enhanced using optical antennas. Bowtie antennas are especially suited because extremely high intensities can be achieved in the gaps. Here, arrays of bowties are characterized as possible candidates for enhancing non-linear processes, including second-harmonic generation (SHG) and two-photon photoluminescence (TPPL) [30]. Based on earlier understanding of the linear response, various arrays were irradiated with a tightly focused laser beam and the resulting signal was analyzed. The dependence of input polarization as well as the nature of the output radiation is examined. Understanding of the relationship between linear parameters of antennas and non-linear response has so far been lacking. Based on near-field simulations and experimental results, a strong dependence of linear properties on the non-linear signal is observed [30]. This allows the ability to controllably design nanostructures for non-linear optical response and extends current understanding of optical antennas for sum frequency generation with potential applications in photovoltaic, sensing and optical communication.

3.3.1 Experimental setup

Antennas with various spacings were illuminated using a Ti:Sapphire laser (80 MHz repetition rate, 100 fs pulse width, center wavelength λ_{pump} = 780 nm) and brought to a focus on the sample in an inverted microscope (Olympus IX81) using a 100X (plan apochromat, numerical aperture of 1.4) oil-immersion objective (Fig. 3.5). The nonlinear emission spectra were acquired in reflection geometry using the same objective, and

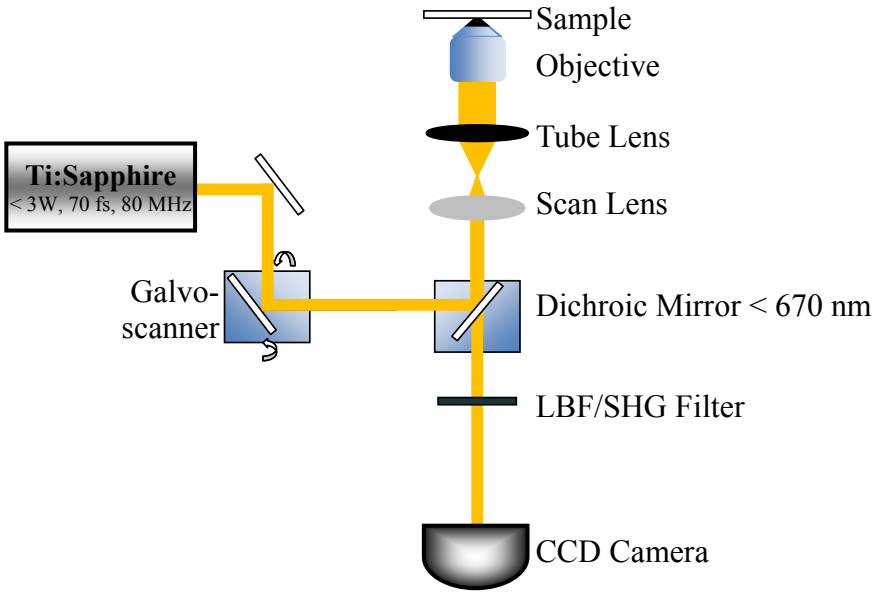

Figure 3.5: Sketch of the setup used for non-linear spectroscopy showing optical path and various components [30].

coupled to a spectrometer (Jobin Yvon CP140-103 grating, Andor DU420A camera) using appropriate ancillary optics, including a 680 nm low-pass filter to reject the pump wavelengths. The spectrometer acquisition parameters were held constant and set to ensure high signal-to-noise ratio for the weakest signal. Prior to each measurement, the z-position of the objective was adjusted using an electron-multiplying charge-coupled device array detector (Hamamatsu C9100-3) and an autofocus program (IPLab 6.0), which uses a Gaussian contrast map to identify the z-position (or axial plane) that produces the highest contrast. Several measures were also taken to minimize laser-induced structural damage due to the sensitivity of the optical properties of antennas to their morphology.

The excitation beam was stochastically scanned using a galvonometer-based scanner (dwell-time less than 150 μs) to achieve relatively uniform illumination. This avoids the comparatively long dwell times and discrete sampling of beam positions

associated with conventional raster scanning and permits the use of higher intensities while reducing the possibility of localized damage due to uneven sample coverage. The input data for the galvanometer-based scanner (Cambridge Technology) was produced at a rate of 7500 Hz using a pseudorandom white-noise generator (LabView). The total size of the scanned area was determined to be ~29 μm X 29 μm. For all measurements shown here, the average power was kept constant at 10 mW (peak power density~10^{12} W/cm^2, peak fluence~32mJ/cm^2) and each measurement was collected from an unexposed area of the arrays with total exposure times (autofocus acquisition) of less than 120 sec.

3.3.2 Non-linear optical response of bowtie arrays

Other studies of similar coupled-dimer nanostructures typically involve intensities around or below 1 mW [3, 78], which is a few orders of magnitude smaller than those used here. The experimentally determined damage threshold was found to be 10 min at 25 mW (measured at the sample) by visual inspection of post irradiation SEM images of the bowties (an example of damage is shown in Fig. 3.3). In addition, a test for optical damage at an average power of 10 mW exhibited remarkable signal stability for over an hour of irradiation.

Figure 3.6 shows spectra collected from arrays of bowties with 500 nm spacing in both directions. Analysis of these data reveals a strong dependence of array spacing, input polarization, and excitation wavelength on the output signal. Of the several important features of these spectra, second harmonic generation (SHG) is most dominant and is observed as a narrowband peak at half the excitation wavelength. A broadband continuum is also observed from ~380 nm until the cut-off of the narrow pass filter (190 nm - 680 nm) suggesting presence of other non-linear processes. For comparison, a Cr

bowtie array with input power as high as 58 mW showed negligibly low SHG counts. Gold film of similar thickness was used as another control sample and no detectable signal was observed, confirming the antennas as the origin of the non-linear response.

For input (horizontal) polarization along bowtie axis (Fig. 3.6 (a)), a much stronger non-linear response is observed compared to vertical polarization (Fig. 3.6 (b)). These figures also show polarization response of the output signal (inset polar plots). While the input and output polarizations for horizontal excitation align well, a 45° mismatch is observed for vertical polarization which is not yet clearly understood.

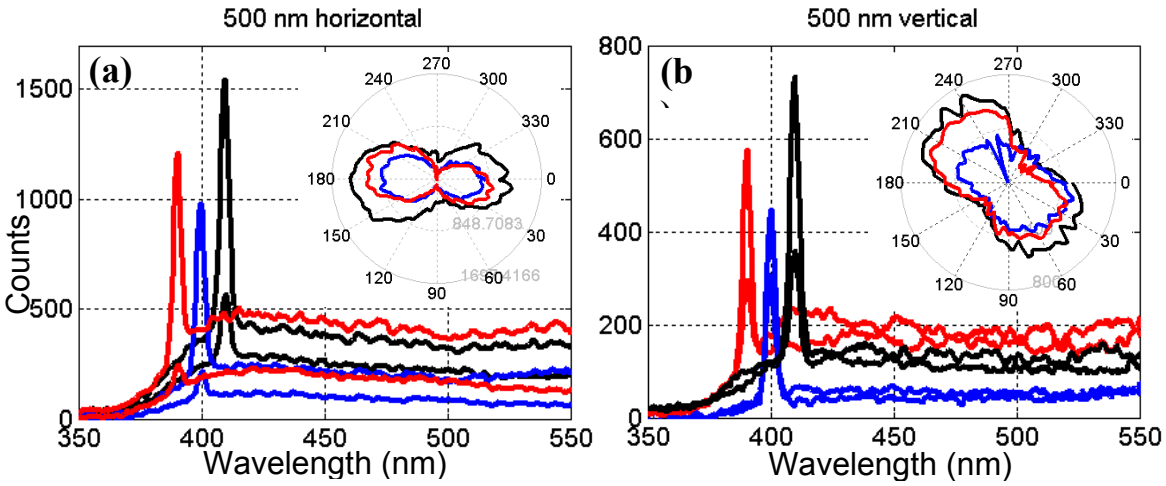

Figure 3.6: Analysis of second harmonic generation (SHG) collected from arrays of bowtie antennas. Representative SHG spectra for arrays with 500 nm spacing at three different excitation wavelengths and two polarizations: input polarization along bowtie axis (a) and normal to bowtie axis (b). Higher (lower) peak spectra are for output polarization parallel (normal) to bowtie axis. Insets show the overall polarization behavior of the radiated SHG signal.

To understand the role of antenna spacing, several arrays were studied. Figure 3.7 (a) shows variation in output signal as a function of array spacing. While the number of particles under exposure reduces with increased spacing, observed SHG signal peaks at around 500 nm suggest strong dependence on the antenna arrangement (Fig. 3.7 (a)). A

direct relationship with linear field enhancement is predicted from the simulation as shown in Fig. 3.7 (b), where the average linear field enhancement has a similar trend as observed in the measurement. This suggests the origin of SHG to be strongly influenced by the linear field enhancement in the bowtie antennas and arrangement of the nanostructure influences the total output signal.

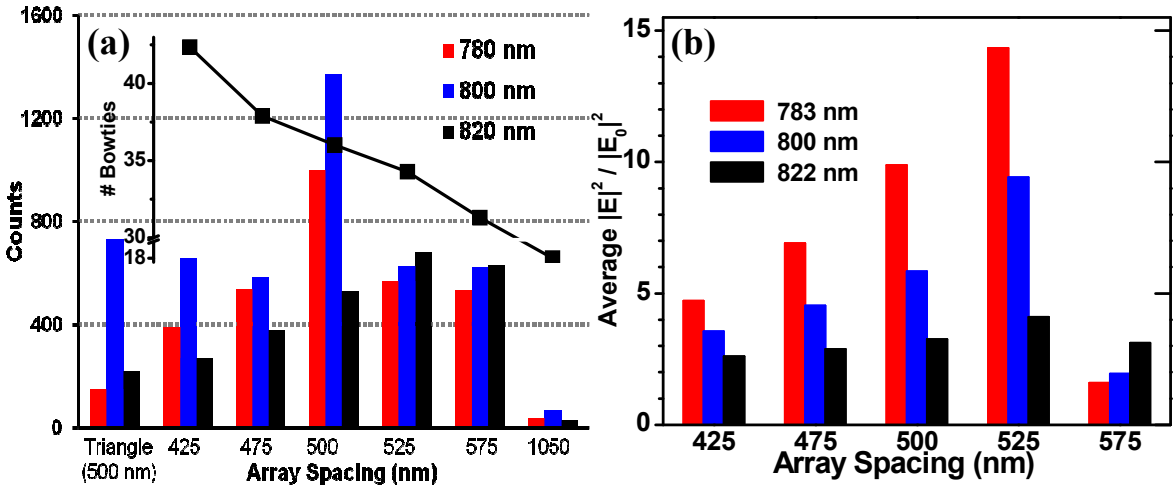

Figure 3.7: (a) Behavior of the collected SHG signal versus spacing at three excitation wavelengths. Maximum signal is observed for 500 nm spacing although particle density decreases with spacing (inset). (b) Similar trend captured for linear response showing simulated average intensity.

To understand the nature of non-linear processes, five spectra for different spacing are plotted in Fig. 3.8. Each spectrum is characterized by an SHG peak, and a broadband shoulder that shows two separate characteristic humps. The Fabry-Pérot resonances in the spectra are due to space between sample and a glass coverslip used to separate index-matching from arrays. To quantify the nature of these signals, intensity of the output signal is plotted as a function of input power at three different wavelengths. As expected, the SHG peak shows a quadratic dependence. The first shoulder plotted at a wavelength of 463 nm also shows quadratic dependence suggesting this response to be

two-photon photoluminescence (TPPL). However, for the second part of the broadband signal, plots at 635 nm show a slope of 1.63 suggesting a completely different kind of white light continuum whose origin cannot be accounted for by using any of the previous studies [3, 35]. Previously reported processes have mostly shown second or fourth order dependence [3]; the latter was not observed in these studies.

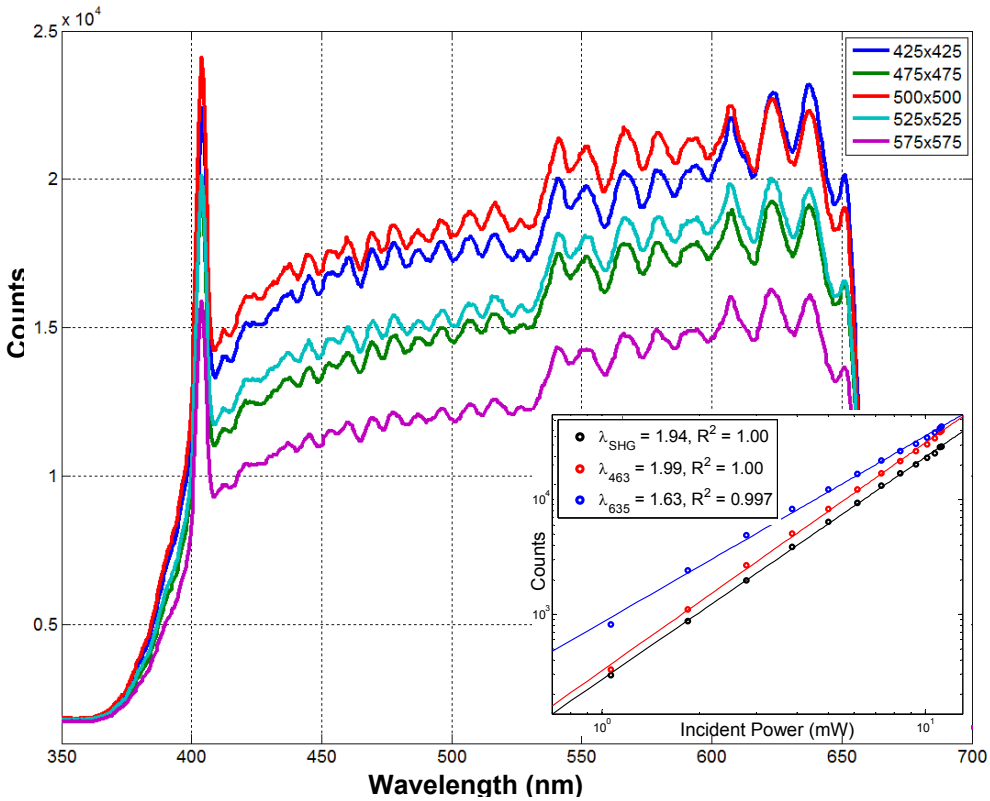

Figure 3.8: Non-linear response of arrays with different spacing shows several characteristic features including second-harmonic generation (SHG), two-photon photoluminescence (TPPL) and a completely new process with power dependence of 1.63 (inset) that has not been observed before.

3.4 Summary

Optical antennas were characterized for several important features including high extinction cross-section, enhanced fields in subwavelength gaps as well as non-linear

signal, all attributed to their unique ability to resonantly couple with the optical excitation source. The linear response was investigated using bright field microscopy and this was complemented with simulations of the near-field behavior. Arrays of antennas were designed and characterized to understand their coupling behavior and blue-shift in resonance was observed compared to single nanostructures. Non-linear spectroscopy of strategically designed arrays showed a very broad light supercontinuum with contribution from second-harmonic generation, two-photon photoluminescence, and a newly identified process with slightly lower than quadratic dependence. The optical characterization allows controllable design of antennas for future applications which will be further investigated using electron-beam excitation in following Chapters.

CHAPTER 4

CATHODOLUMINESCENCE IMAGING OF ANTENNAS

4.1 Introduction

Recent progress in optical antennas is attributed to their ability to couple propagating radiation into confined electromagnetic fields. These extremely high fields confined within sub-wavelength regions result in hotspots that hold promise to revolutionize several areas including single molecule sensing [21-23] and low power thresholdless nanolasing [79-81]. Highly localized optical modes can be engineered by patterning metal films and nanostructures into unique shapes and sizes. Exciting and imaging these modes require state-of-the-art techniques, e.g., near-field scanning optical microscopy (NSOM) [40, 82], electron energy loss spectroscopy (EELS) [42, 43, 83-85], and cathodoluminescence (CL) spectroscopy [42, 44-46, 51-53, 86-95]. Among these, CL is advantageous because of its high resolution, ease-of-excitation, and less stringent demands for sample preparation. The electron beam offers all the possible wave vectors, especially for plasmon excitation near the flat band region of dispersion relation which is an important constraint for optical excitation.

CL has previously been used to study optical modes of nanowires [88], plasmonic disks [44, 89-92], and nano-antennas [45-46]. However, designing nanostructures on substrate that do not interfere with antenna resonance is a major challenge. In this chapter, a new approach to design, excite and study optical modes of triangular nano-antennas is reported. A series of fundamental modes including out-of-plane, in-plane and high-order modes are characterized.

The optical behavior of polarization-independent triangular nano-antennas changes dramatically when a second triangle is brought in proximity to form a bowtie dimer, as reported in Chapter 3. Hybridization of the triangle modes [54] results in new modes that are strongly dependent on the nature of the excitation source. The high-energy "dark" or "anti-parallel" modes cannot be excited using a plane wave source [51, 96] due to weak coupling with the subwavelength sized nanostructures. However, the localized electron-beam in CL allows excitation of both "bright" (or "parallel") as well as "dark" modes. Spectral and monochromatic imaging of these bright and dark modes is supported using finite-difference time domain (FDTD) simulations. The bright modes are strongly dependent on antenna loading, which can be modified by changing the size and index of gap between the two triangles. Simulations and theoretical studies are provided to support the experimental observations.

4.2 Fabrication of low index and minimal background substrates

4.2.1 Fabrication approach

An important challenge for CL is the strong luminescence from substrate that can overshadow any possible antenna modes. Most commonly used materials in optics and device processing show luminescence under electron excitation, making the nature and purity of the substrate critical. As an example, float glass shows eight peaks in visible spectrum [94] making it nearly impossible to distinguish any optical antenna peaks. One possible solution is to use high purity materials, e.g., Si, InP, or other single crystals that do not show any peaks in the visible region; however, the high refractive index of these

materials shifts dipole peaks beyond the detection range of the setup [46]. Since the resonance wavelength of an antenna is directly proportional to its size and index of underlying substrate, an increased index value requires comparable reduction in size. The typical size of optical antennas is ~100 nm or less and any further reduction is beyond the reach of most fabrication techniques; hence any reduction in index can significantly help nano-antenna studies.

To reduce the background luminescence, a 100 nm thick gold film was first deposited on Si substrate, followed by another 100 nm thick silicon oxide (SiO_2) layer. SiO_2 also shows two peaks in visible and near-IR spectrum [95]; however, the high energy peak lies outside the dipole peaks of current designs (and was observed to be relatively weaker for the PECVD deposited oxide used here), while the low energy peak is red-shifted from the antenna peaks. 50 nm thick Au nanostructures were fabricated on this multilayered substrate using electron-beam lithography. Subsequently, the oxide outside nanostructures was removed using standard reactive ion etching (RIE) process (PlasmLab Freon-RIE with 60 sccm flow rate of CHF_3, at a pressure of 35 mTorr and 90W power). For further undercutting of the oxide underneath the nanostructures, 50:1 H_2O:HF wet etching solution was used. This etching step was carefully controlled until the gold triangles were about to fall off the oxide nanostructures.

A schematic of the CL setup in Fig. 4.1 shows SEM image of 50 nm thick Au triangles with undercut region clearly visible. As can be seen from the right triangle, SiO_2 structure has shrunk and is smaller than the Au triangle due to selective wet etching. Beside this shrinking, the solution appears to etch the Au-SiO_2 interface faster than bulk oxide, as seen from the extra etching of exposed interface on the left triangle and results

in a very small contact area. An overall effect of this etching behavior on the antenna is that most of it is surrounded by vacuum, except the small bottom contact with oxide. This translates into an effective index close to vacuum and lower than the average value expected from a flat substrate. Additionally, the gold film underneath helped suppress background noise from the native oxide once the top oxide was etched away. The effect of the gold layer on the antenna modes should be minimal since the oxide is thick enough to prevent any significant interference with the nanostructures as reported earlier [89].

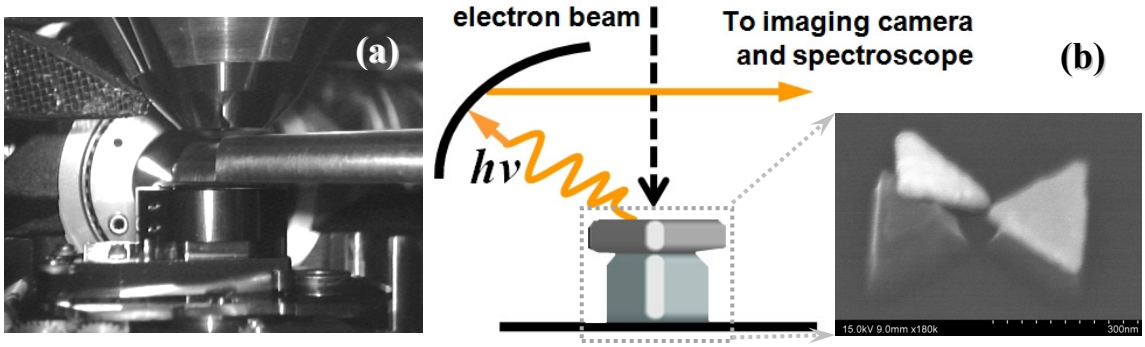

Figure 4.1: Experimental setup: (a) inside view of SEM based CL setup with parabolic mirror mounted between the electron-beam column and sample holder; (b) schematic of the setup and an SEM image of nano-antenna dimer after RIE and wet etching.

To understand how nano-antenna resonance is modified by substrate index, FDTD simulations were carried out for several indices. Figure 4.2 plots resonance peaks as a function of substrate index for two triangles with tip-to-base height of 120 and 150 nm, excited using a plane wave source incident normal to the antenna surface. The narrow window of substrate index in which peaks lie in the visible spectrum highlights the importance of substrate index in optical antennas. The change in overall index by lifting up the Au nanostructure is also considered. For simplicity, no undercutting from the wet etching step is considered. For a 150 nm triangle sitting on SiO_2 (n=1.5) layer, the

simulated peak lies at 700 nm. However, it shifts to 680 nm when the outside oxide is removed and the Au triangle is sitting on a 100 nm thick SiO_2 triangle of the same size. Further blue-shift should be expected when undercutting from wet etching is considered.

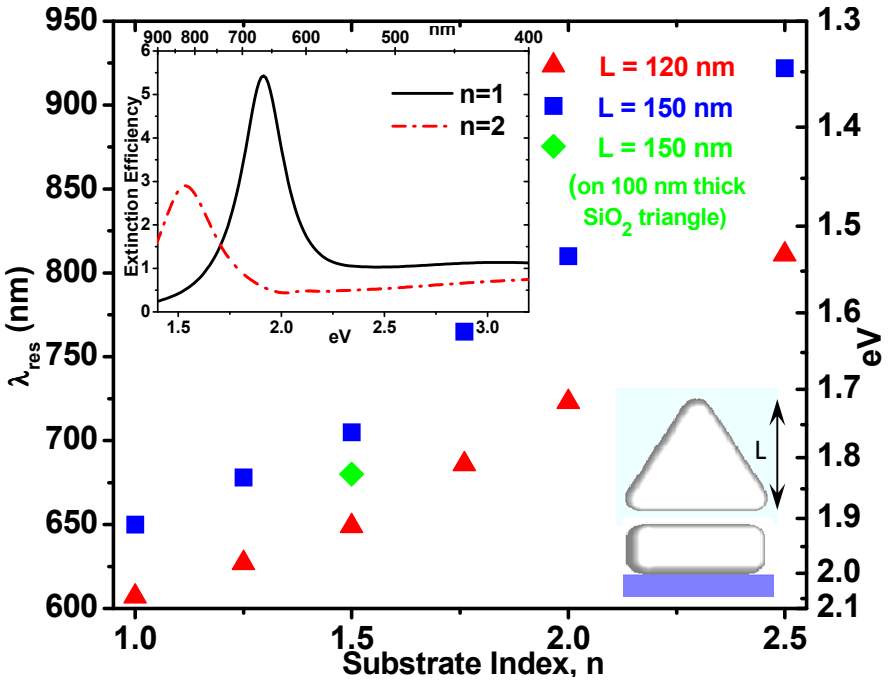

Figure 4.2: Resonance wavelength of Au triangles as a function of substrate index and role of lifting up of the nanostructures in lowering the effective index using an oxide triangle (before wet etching). Inset shows extinction curves for two substrate indices. 15 nm radius of curvature was used for the triangles as observed in fabricated samples.

4.2.2 Experimental setup

CL measurements were carried out on a commercial setup (from Gatan, Inc.) attached to a scanning electron microscope (JEOL 7000F SEM) [45-46]. This system has an aluminum parabolic mirror (see Fig. 4.1) that directs the collected photons into a photospectrometer coupled to a Czerny-Turner type monochromator for spectral sensing. The spectra and images were collected using a photo-multiplier tube (PMT) with a range of 250 nm to 900 nm. For all the studies reported here, electron accelerating voltage of 30

kV and currents of 5-50 nA were used (otherwise mentioned). For spectra, photons were collected for 500 ms/nm (with spectral spacing of 2 nm) while during monochromatic imaging, photons were collected for 1 ms/pixel for a total collection time of 4.5 minutes (512x512 pixel images). Both monochromator slit openings were set at 3.7 mm which corresponds to a spectral resolution of approximately 10 nm. All the spectra were corrected for grating response function; however, no background subtraction was required due to reasonably high signal-to-noise ratio for these multilayer substrates.

4.2.3 Simulation of electron beam excitation

FDTD simulations of electron-beam excitation of nano-antennas shown in Fig. 4.3 (a) clearly highlight the importance of low index substrate. The beam was modeled as a series of dipoles with a temporal phase delay based on electron velocity. Si was considered as a dispersive medium with data for Au taken from Palik [97].The two plots compare a 120 nm triangle sitting directly on a flat Si surface with another triangle that is lifted up by a 100 nm thick SiO_2 triangle of the same size. For simplicity no undercutting is considered in the simulations. The high intensity peak for the Au triangle sitting on oxide triangle falls within the range of the CL detector and is about 15 times stronger than the flat Si substrate. This enhancement can be understood by considering the fact that when the antenna is sitting close to a high index substrate, most of the light will be radiated into the high-index substrate; lifting up and undercutting allows more of the light to radiate away from substrate. The blue-shifted low intensity peak observed for Au on Si substrate indicates this peak is possibly from one of the higher order modes while the dipole mode has shifted beyond the detection range.

4.3 Modes of triangular nano-antennas

4.3.1 Excitation using raster scanning of electron-beam

Figure 4.3 (b) shows the spectrum of a gold film (black curve) taken as a reference using excitation voltage of 30 kV and beam current of 100 nA. A peak at 520 nm is observed which has earlier been attributed to the surface plasmons of gold [93]. For these preliminary measurements, no gold layer below the oxide was used. Measurement on SiO_2 around the antennas shows two prominent peaks (gray) of the oxide as expected [95]. Raster scanning of a 50 nm thick Au triangle (red curve) with length L = 150 nm shows a peak at 575 nm. This peak does not match with the simulated in-plane modes shown earlier in Fig. 4.2, and is therefore attributed to an out-of-plane dipole mode. Similar observation has earlier been reported for this mode in Ag nano-triangles [45]. For comparison, the spectrum taken on a triangle directly sitting on Si substrate (blue) shows a weak peak at higher frequency, as suggested in simulations.

Panchromatic images were collected to understand the spatial distribution of hotspots associated with these modes. A CL image taken by raster scanning of the electron beam at 30 kV and 85 nA shows high-contrast tip modes as seen in the inset of Fig. 4.3 (b). The contrast for low index configuration was observed to be much higher compared to Si substrates. These panchromatic images were used to find the spatial resolution of the CL imaging technique as reported earlier. From images of closely spaced triangle dimers a value of approximately 22 nm (FWHM) was derived, which is comparable to the previously reported value [44].

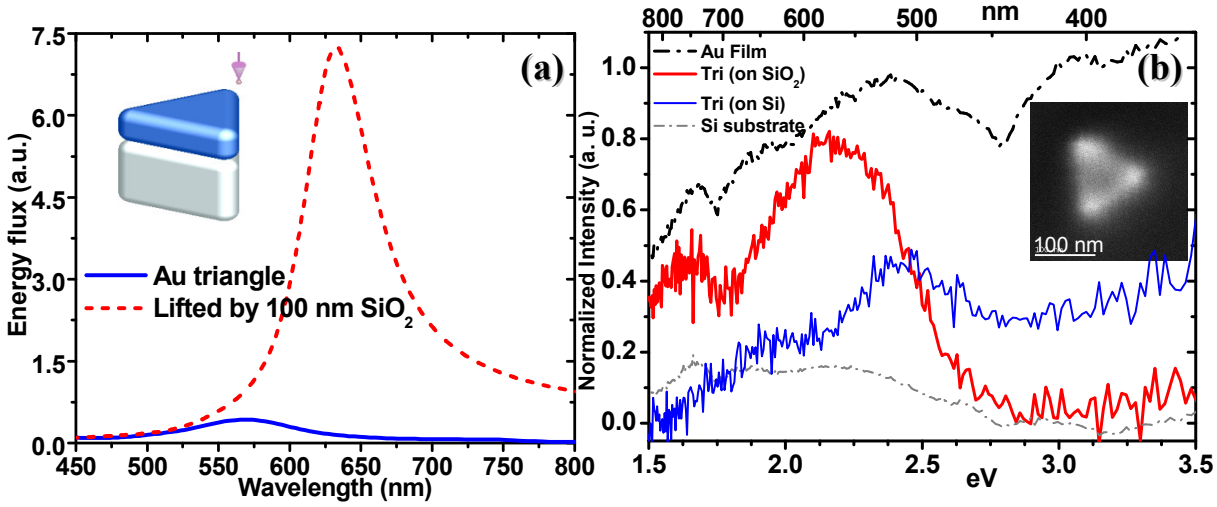

Figure 4.3: (a) Simulation showing effect of raising the antenna above the Si substrate using a 100 nm thick SiO_2 triangle. More radiation coupled out for the raised triangle when excited using an electron-beam 10 nm away from the tip; (b) spectra from raster scans measured at different locations of the sample and a panchromatic image of Au triangle (inset) showing the dominant emission is from tips. Note that no gold film underneath the oxide layer was used in this sample.

A more rigorous analysis of triangle resonance behavior as a function of size is considered in Fig. 4.4. Five triangles of different sizes with resonance peaks across the visible spectrum were measured. Figure 4.4 (a) shows spectra taken by raster scanning of electron-beam. Strong resonant peaks that are dependent on the particle size are observed. When plotted against triangle size (Fig. 4.4 (b)), a linear relationship similar to plane wave excitation (as reported in Chapter 2) is clearly observed. Monochromatic images of one of the triangles (inset image in Fig. 4.4 (b) corresponding to black arrow in (a)) shows strongly luminescent tip modes. For 175 nm triangles, the dominant peak lies outside the range of PMT; however, a second blue shifted peak is observed. A monochromatic image taken near this peak, and marked using a red arrow in Fig. 4.4 (a) shows strongly luminescent edges, suggesting excitation of higher modes of the triangular nano-antennas. Spectra taken on top and bottom gold layers are also plotted for comparison.

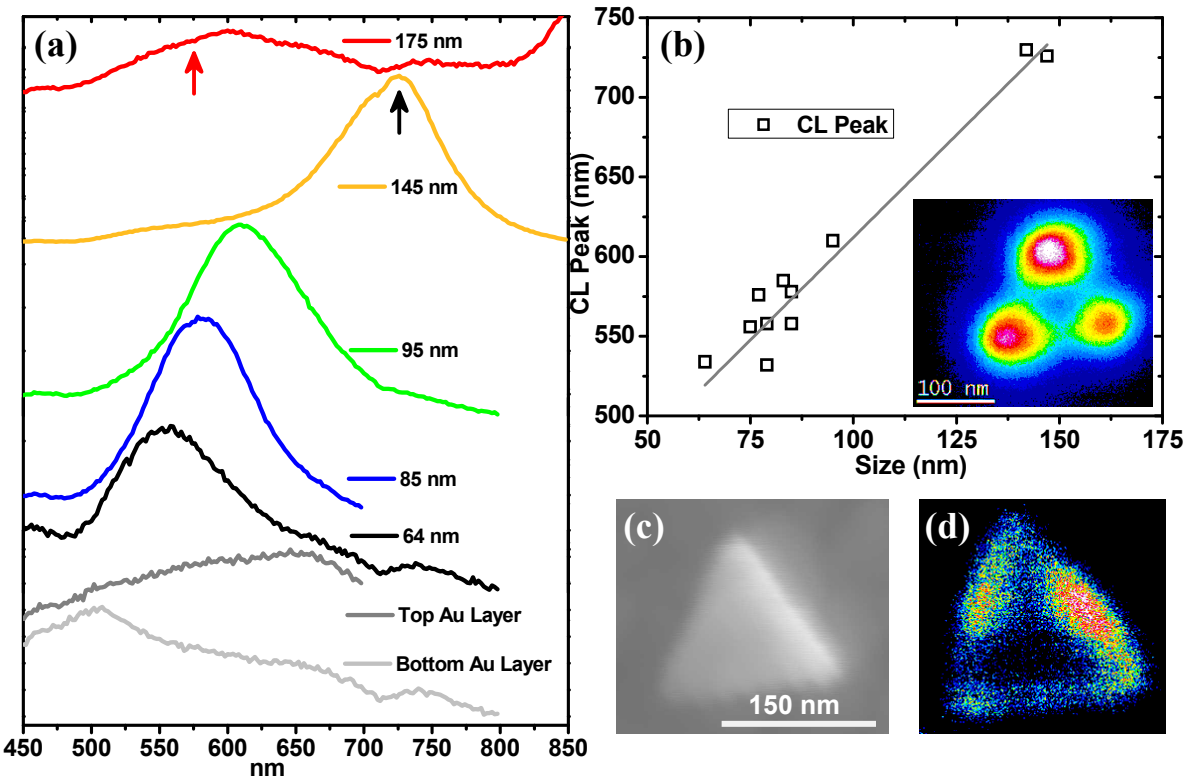

Figure 4.4: Excitation of triangular nano-antenna modes using raster scanning of electron-beam. (a) Spectra plotted for triangles of various sizes show strong dipole peaks as well as higher modes for larger triangles. (b) A linear relationship is observed between resonance peaks and triangle sizes; inset shows a pseudo-color monochromatic image (taken for 145 nm triangle at black arrow in (a)) and suggests these dominant peaks correspond to tip modes. (c) SEM image of 175 nm triangle whose dominant peak lies outside the spectral range; however, monochromatic image taken in (d) at 575 nm (red arrow in (a)) shows a higher mode corresponding to edge mode.

4.3.2 Excitation using fixed electron-beam

So far only raster scanning of the antennas lying flat on the substrate is considered; however, excitation using localized beam with different orientations of the antenna can further help in exploring their optical behavior. For this purpose, two approaches are considered. In the first approach, excitation using a localized beam has been shown to excite completely different modes based on the beam location [43, 63, 83]. Figure 4.5 shows three spectra taken for a 110 nm triangle by localizing the beam near

tip, edge, and at the center. The lowest energy peak corresponds to tip modes as reported earlier [43, 63]. However, the edge and tip modes are relatively closer than what has been reported earlier. Since the center mode is difficult to excite, this peak might be due to the out-of-plane mode.

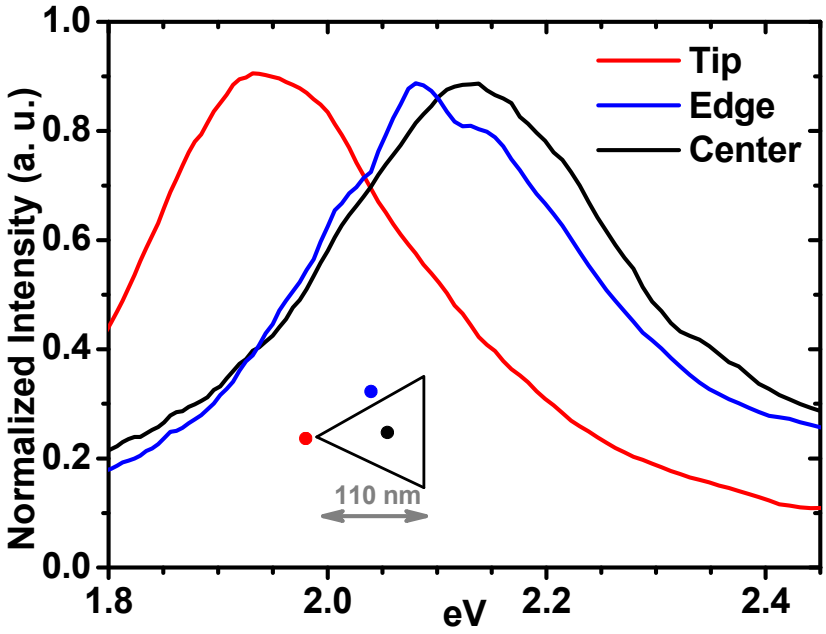

Figure 4.5: Spectra of various modes excited using a localized electron beam placed 10 nm away from tip and edge, and at the center of a 110 nm triangle.

In the second approach, the triangles were tilted by further undercutting the oxide. This allowed excitation of antenna modes by glancing angle incidence of the electron-beam close to the antenna surface. Figure 4.6 (a-d) shows a schematic of this approach as well as imaging of a triangle that has fallen off the SiO_2 pillar. The SEM images confirm positions of the two triangles and panchromatic imaging clearly shows location of hotspots on the Au triangle. For a fully tilted triangle with 90° rotation, glancing angle excitations are shown in Fig. 4.6 (e-g). The in-plane dipole mode excited in this configuration by a beam localized 10 nm away from the antenna (blue dot) shows

excellent match with the simulated spectrum. The additional peaks appear due to the Si/SiO_2 background as can be seen from the gray curve taken over the SiO_2 nanostructure. The relatively wider peak of the CL spectra is possibly due to broadening of the excited mode when the triangle is not fully oriented in the vertical direction and will be affected by fabrication imperfections. Additionally, the simulated particle has a vacuum surrounding resulting in narrower peaks, while the experimental peak width will increase due to the Si substrate at the bottom. The electric field 2 nm away from the opposite interface shows a resonance behavior similar to plane-wave excitation, confirming the experimental observation.

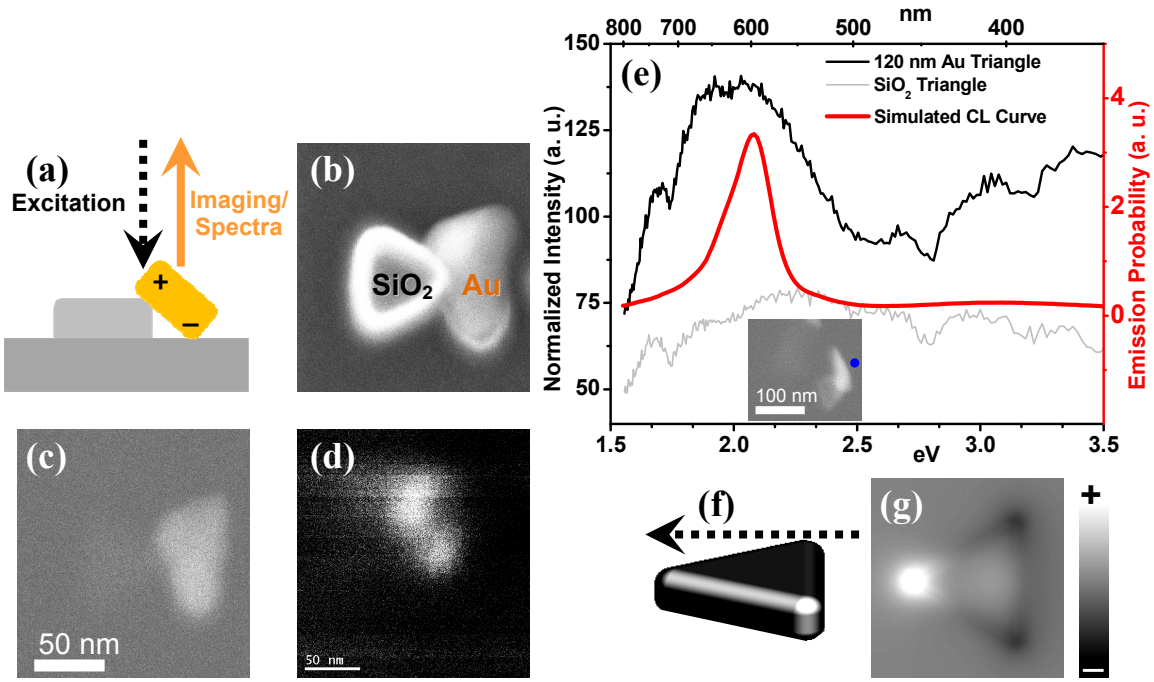

Figure 4.6: Excitation of antenna modes by tilting the nanostructures. (a) shows schematic of the approach; (b) secondary electron image and (c) backscattered electron image confirming the tilted Au structure fallen after over-etching of the oxide; the backscattered electron image only resolves the high atomic materials. (d) Panchromatic image showing the strongly luminescent tips of triangular antenna; (e) measured and simulated spectra for a 90° tilted triangle excited using a localized beam 10 nm away from surface (blue dot); (f-g) show simulated field profile for a beam parallel to the surface (marked with arrow) plotted 2 nm away from the opposite surface.

4.4 Dimer modes: dark and bright modes of a bowtie antenna

4.4.1 Theory of parallel (bright) and anti-parallel (dark) modes

The bowtie nano-antenna supports both parallel and anti-parallel dipole modes [96, 98-102] on the two identical metal nanoparticles due to hybridization between their dipole modes. The single particle dipole modes are particularly interesting because of the triangular shape. Although it is not intuitively obvious, it can be shown that an equilateral triangle supports two-fold degeneracy of its in-plane dipole modes because of its 3-fold rotational symmetry [74]. When the two identical equilateral triangles are brought closer to form a bowtie nano-antenna, it breaks the 3-fold rotational symmetry. Such broken rotational symmetry separates the two modes and each mode hybridizes with the corresponding mode on the other particle, forming four new plasmon modes: two bright modes and two dark modes. The bright modes correspond to the case where two dipoles are parallel to each other while the dark modes correspond to anti-parallel dipoles. For further understanding of their interaction, Fig. 4.7 shows the charge profile for the horizontal case.

Such hybridization of plasmon modes can be qualitatively modeled using dipole approximation for each nano-triangle. First, suppose a single nanotriangle has a dipole polarizability for each of the in-plane polarizations (along x and y axes) and is under the influence of an external electric field, $\mathbf{E}^{inc} = E_x^{inc}\mathbf{x} + E_y^{inc}\mathbf{y}$:

$$\begin{pmatrix} p_x \\ p_y \end{pmatrix} = \begin{pmatrix} \alpha_x & 0 \\ 0 & \alpha_y \end{pmatrix} \begin{pmatrix} E_x^{inc} \\ E_y^{inc} \end{pmatrix}, \tag{4.1}$$

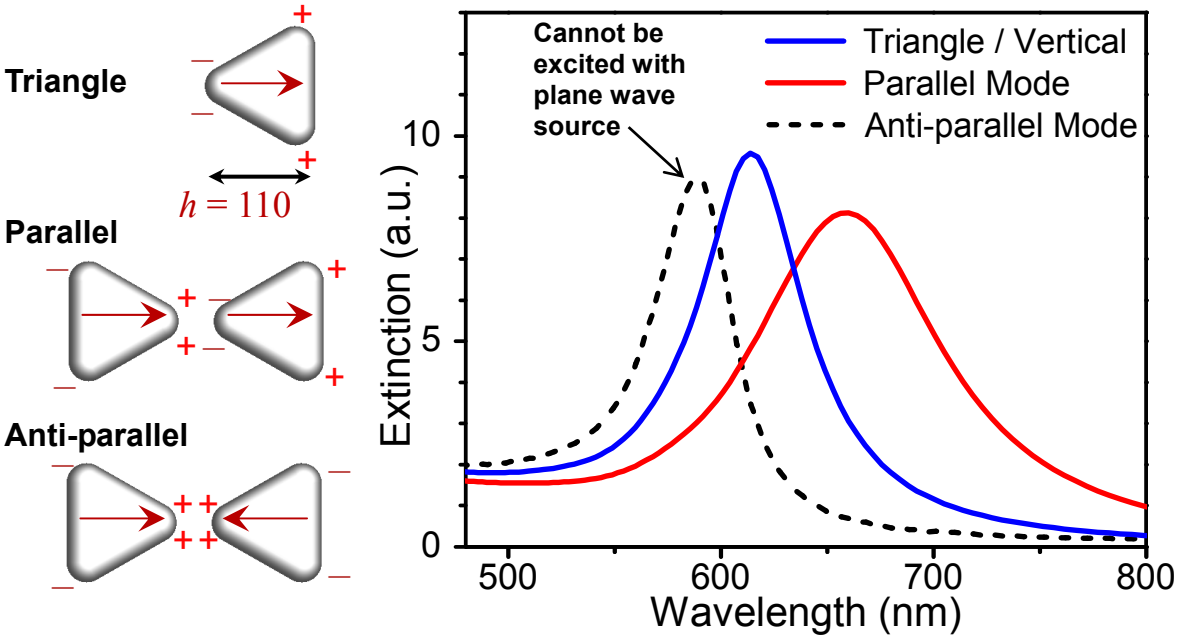

Figure 4.7: Simulated plane wave excitation of triangle and bowtie modes, with charge profiles for horizontal modes. The two vertical and triangle modes are degenerate. The anti-parallel mode (dashed line) cannot be excited with a plane wave source.

where p_x and p_y are the dipole moments in x and y directions, respectively. Due to the 3-fold rotational symmetry, the polarizability tensor is preserved under 120° rotation:

$$\begin{pmatrix} \frac{1}{2} & -\frac{\sqrt{3}}{2} \\ \frac{\sqrt{3}}{2} & \frac{1}{2} \end{pmatrix} \begin{pmatrix} \alpha_x & 0 \\ 0 & \alpha_y \end{pmatrix} \begin{pmatrix} \frac{1}{2} & \frac{\sqrt{3}}{2} \\ \frac{\sqrt{3}}{2} & \frac{1}{2} \end{pmatrix} = \begin{pmatrix} \alpha_x & 0 \\ 0 & \alpha_y \end{pmatrix}, \tag{4.2}$$

which implies $\alpha_x = \alpha_y$. This verifies that the two in-plane dipole modes are degenerate. When two equilateral nano-triangles are placed in tip-to-tip configuration to form a bowtie, the dipole moments on the two nano-triangles are coupled together and can be described by:

$$\begin{pmatrix} \alpha^{-1}(\omega) & -g_\sigma(\omega, d) \\ -g_\sigma(\omega, d) & \alpha^{-1}(\omega) \end{pmatrix} \begin{pmatrix} p_{1,\sigma} \\ p_{2,\sigma} \end{pmatrix} = \begin{pmatrix} E_{1,\sigma}^{inc} \\ E_{2,\sigma}^{inc} \end{pmatrix}, \tag{4.3}$$

where σ = *x* or *y* denotes the polarization, g_σ is the coupling constant, α is the in-plane polarizability of particle, *d* is the distance between two dipoles, and $p_{1,\sigma}$ ($E_{1,\sigma}^{inc}$) and $p_{2,\sigma}$ ($E_{2,\sigma}^{inc}$) are, respectively, the σ-components of the first and second dipoles (the incident fields on the first and second dipoles). It should be noted that there is no cross-polarization coupling between *x* or *y* components. Non-trivial solutions to the source-free coupled dipole equation require

$$\alpha^{-1} = \pm g_\sigma . \tag{4.4}$$

Here, "+" and "–" denote the solutions for parallel and anti-parallel dipoles, respectively. The corresponding complex frequencies $\Omega_r^\pm = \omega_r^\pm - i\Gamma^\pm$ (where $\omega_r^\pm$ and $\Gamma^\pm$ are real numbers) satisfying Eq. (4.4) can be approximated by:

$$\omega_r^{\pm 2} \approx \omega_0^{\,2} \mp f\,\mathrm{Re}(g_0) - (\Gamma^\pm)^2 . \tag{4.5}$$

Here, the decay rate $\Gamma^\pm$ is approximated by

$$\Gamma^\pm \approx \Gamma_0 \pm \frac{f}{2\omega_0}\mathrm{Im}(g_0) , \tag{4.6}$$

and $g_0 = g_\sigma(\Omega_r^\pm, d)$.

In these expressions for the resonance frequencies of the two modes, $\omega_r^\pm$, and their corresponding decay rates, $\Gamma^\pm$, "+" and "–" indicate the case of parallel and anti-parallel dipoles, respectively, ω_0 is the original single nano-triangle resonant frequency (excluding the damping red-shift), Γ_0 is the decay rate for single nano-triangle, g_0 is the coupling constant at the resonant frequency; and *f* represents the strength of single nano-triangle resonance. Eq. (4.5) applies to both longitudinal mode (dipoles parallel to the

dimer axis) and vertical mode (dipoles perpendicular to the dimer axis). For the longitudinal modes in the quasistatic limit (wavelength >> size of nanobowtie), Re(g_0) is positive (negative) for parallel (anti-parallel) dipole mode and, therefore, it reduces (increases) the resonant frequencies. Such red-shift and blue-shift can also be interpreted as the results of reducing and increasing the restoring force of the oscillators by the charges on the adjacent particles, respectively. In addition to the shift in frequency, we can also see from Eq. (4.6) that the decay rates change after the hybridization. Since Im (g_0) is also positive in this case, the decay rate of the parallel (anti-parallel) dipole mode becomes higher (lower) after the hybridization. For the vertical modes, the sign of Re(g_0) is just opposite to that of the corresponding longitudinal mode while that of Im (g_0) is the same. This gives opposite spectral shifts after hybridization when compared with the longitudinal case. However, the shift is much smaller for vertical modes because of the relatively weaker coupling. The centers of dipoles for the vertical modes are more separated due to the tendency to have induced charges concentrated at the corners. The parallel and anti-parallel vertical modes are thus almost "degenerate" and it is difficult to distinguish them in spectra due to the large linewidths of surface plasmon modes.

4.4.2 Simulation of dark and bright modes

Figure 4.8 shows simulations of various modes and their field profiles excited using an electron-beam source. When the beam is focused 10 nm away from outside tip (case D in Fig. 4.8), the excited mode overlaps with single triangle mode, suggesting excitation of the vertical modes that degenerate with triangle mode. The field profile for this configuration shows most of the fields are concentrated around outside tips while very small fields at the gap are observed resulting from triangle interaction. When the

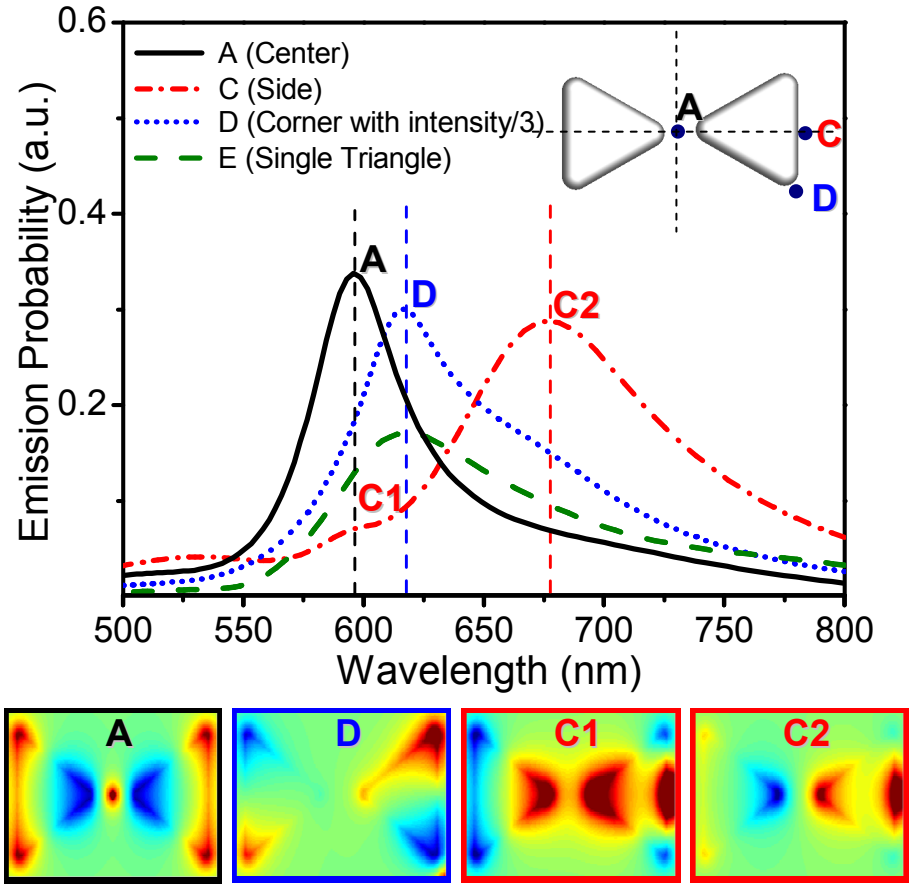

Figure 4.8: Simulations of electron-beam excitation of triangle and bowtie modes, with corresponding field profiles shown for the bowtie (110 nm size and 35 nm gap). Excitation near outside tip (D) of the bowtie excites vertical modes that degenerate with triangle mode as suggested from the field plots. Electron-beam fixed in the gap excites a blue-shifted anti-parallel (dark) mode (A) while excitation near the right edge shows two peaks (C1, C2), with dominant peak corresponding to the parallel (bright) mode (C2).

beam is focused in the gap (case A), a blue-shifted mode with fields of the same polarities around the gap is observed. This field profile clearly shows that this is anti-parallel (dark) mode. However, when the beam is fixed near the outside edge of triangles (case C) a red-shifted mode is observed. The field pattern shows opposite polarities (C2) around the gap clearly indicating excitation of parallel (bright) mode. This configuration also has a weak peak at the same wavelength as the gap excitation, suggesting both dark (C1) and bright (C2) modes are observed.

Experiments carried out on bowties of 110 nm with 35 nm gaps confirm the simulated prediction of the various modes. Figure 4.9 shows three curves for the beam locations shown near the bowtie image (inset). The bright mode for this large gap is relatively weak and shows small signal; however, both the modes for the edge excitation are clearly observed.

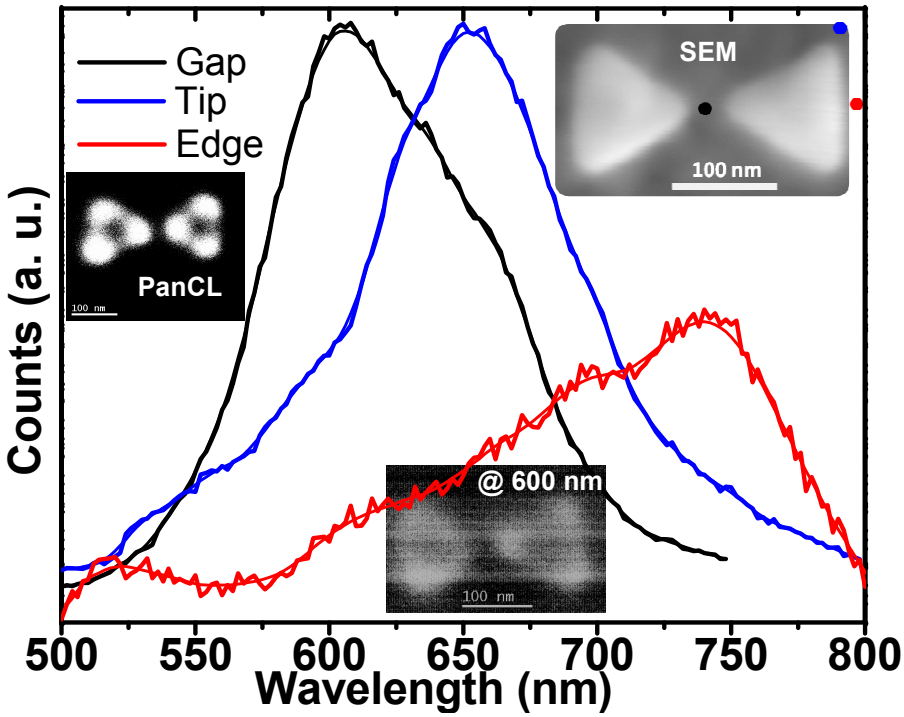

Figure 4.9: Experimental spectra of the dark and bright modes observed using localized beam excitation at various locations near the bowtie. The bowtie has tip-to-base height of 110 nm and triangle separation of 35 nm. The lines are average fits of the measured spectra. Panchromatic and monochromatic (at 600 nm) images are also shown.

4.4.3 Effect of gap size

The hybridization model predicts a strong dependence of nano-triangle separation. However, both modes are not affected in similar manner. Figure 4.10 shows the effect gap size on the two modes for a 75 nm bowtie. There is a strong dependence of gap size on parallel (bright) mode, with almost 50 nm blue-shift as the gap is increased from 5 nm

to 50 nm. For sub-10 nm gaps the shift is seen to be increasing dramatically; however, for larger separations the shift saturates very rapidly. The effect of gap size on anti-parallel mode is almost negligible, with <5 nm shift over a similar range. Figure 4.10 also indicates that as the separation is increased, the two modes will approach to single triangle mode. This behavior agrees with the previously reported observations on effect of loading on antenna resonance [40].

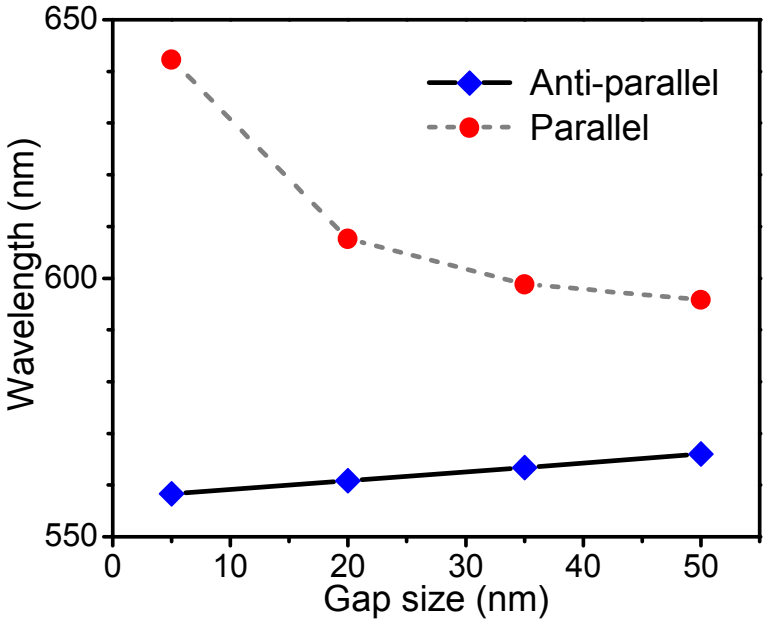

Figure 4.10: Effect of gap separation on the parallel (bright) and anti-parallel (dark) modes of a 75 nm bowtie. For larger separations, the two modes approach a single triangle resonance mode.

4.4.4 Effect of antenna loading

A similar effect should be observed for different antenna loading. Alù and Engheta have shown [10] that changing the antenna loading can dramatically affect the antenna behavior. By changing antenna index, the bright mode shows a significant shift similar to what is observed during decreasing triangle separation. For two nano-rods of 5 nm radius and separated by 3 nm gap, changing the loading from air (n=1.0) to SiO_2

(n=1.5) shows about 50 nm red-shift. Similarly, filling the gap with Si_3N_4 (n=2.0) results in ~110 nm shift. The peaks can be further shifted; however, these shifts are always coupled with proportionally weaker resonances and therefore might make it difficult to excite the nanostructures.

To confirm the above behavior with a bowtie antenna, the gaps were loaded using a thin layer of Al_2O_3 deposited using atomic layer deposition (ALD). This approach allows filling of the gap with conformal coatings of very high quality dielectric films having a relatively low index (n=1.76). With this index value, a reasonable peak shift should be observed without compromising the resonance behavior. However, the observed shift should be slightly higher than with loading alone because ALD coats the whole antenna and there will be some extra shift coming from the dielectric on the antenna arms. Figure 4.11 shows SEM images of a 75 nm bowtie before and after 5 nm Al_2O_3 coating. The corresponding spectra taken by excitation using an electron beam localized near the edge show an approximately 70 nm peak shift.

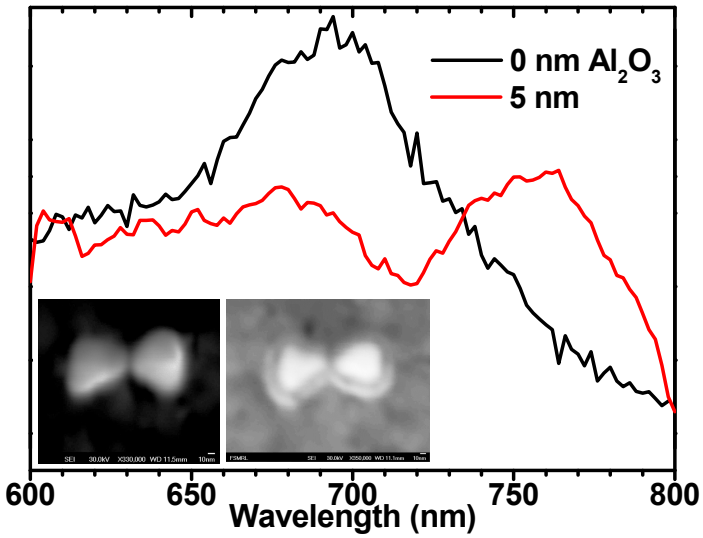

Figure 4.11 Effect of antenna loading on the bright mode excited using an electron beam localized 10 nm away from the right edge. Inset show SEM images of the same bowtie before and after 5 nm Al_2O_3 (n=1.76) ALD coating.

4.5 Summary

Cathodoluminescence (CL) imaging spectroscopy is a unique technique to characterize and map antenna behavior. Preliminary analysis of triangle modes showed a strong substrate dependence on their resonance behavior. A new approach involving deposition of thin gold and silicon oxide layers below the antenna and subsequent etching away of the oxide outside the antennas resulted in low-index and low background luminescent substrates. Characterization of gold nano-triangles showed a linear dependence of resonance peak on their size, with fields strongly enhanced near the triangle tips. By placing another triangle nearby, strong hybridization of the triangle modes was observed resulting in parallel (bright) and anti-parallel (dark) modes. For the first time, these modes were mapped using cathodoluminescence spectroscopy and the results showed excellent matching with simulations. A strong dependence on the particle separation and gap index was observed as predicted by earlier reports.

CHAPTER 5

CATHODOLUMINESCENCE IMAGING OF NANO-DISKS

5.1 Introduction: Nano-disks as λ-size antennas

Most of the efforts in previous chapters have been devoted to studies involving subwavelength antennas with characteristic dimensions close to 100 nm. The nanostructures probed here are comparable to their resonance wavelengths with typical dimensions ranging between 50 nm to all the way up to 1 μm. These plasmonic nano-cavities with very small mode volumes offer thresholdless laser operation by combining spontaneous emission with the lasing mode [79-81, 103-106]. The ultrasmall optical devices are of interest because of their low power consumption and possibility of large-scale integration into current electronic devices and future all-optical systems [107]. They are important candidates for studying exciton-photon interaction and cavity quantum electrodynamics [107]. Nano-cavities can be potentially used as single photon sources that are important for quantum computing and highly secure optical communication; however, these sources require high efficiency, low multiphoton probability, and quantum indistinguishability [107-108].

Conventional microdisk lasers rely on total internal reflection at the walls for the whispering gallery modes with very high quality factor [108]. However, for plasmonic nano-disk resonators with very small mode volume, the lowest-order modes are TM (1, 1) modes with enhanced fields at the edges [53]. As the size of the disk increases, more azimuthal and radial modes can be supported. Additionally, it has also been shown that degenerate whispering gallery (WG) modes dominate for larger disks [109], and can

show significant mode splitting, e.g., due to structural imperfections [110]. The nature of these WG modes and the role of disk geometry on mode profile, field enhancement and mode splitting are not well understood. In the current studies, electron-beam excitation is used to probe some of these modes on gold and silver nano-disks. As observed in Chapter 4, CL provides the capability to map the highly localized modes of the disks. By fixing the beam at specific locations of the nano-disk, individual modes can be selectively excited. The samples in these studies were coated with a 2 nm thin Al_2O_3 layer using atomic layer deposition (ALD) to reduce the damage from high velocity electrons. Gold was found to be less susceptible to such damage, and studies requiring repetitive scans on the same disks were carried out on Au samples. This helped avoid any effects such damage might have on the characterization.

5.2 Plasmonic modes of nano-disks

Parametric studies of Ag nano-disks show they can sustain several modes depending on their size. Panchromatic images of 50 nm thick Ag disks shown in Fig. 5.1 (a) reveal these modes. For smaller disks up to 150 nm diameter, single TM (1, 1) modes with high luminescence from the edges are observed. As the size of the disk increases, more modes start to appear with predominantly bright center. By fixing the electron-beam at the center of disks, these Bessel modes can be selectively excited. Spectra shown in Fig. 5.1 (b) show several peaks from this excitation. Beside the bulk mode of silver near 330 nm [44], a strong peak is observed that red-shifts with increasing disk diameter as plotted in Fig. 5.1 (c). With larger disks, higher modes can also be excited resulting in more peaks but fewer counts per mode. This behavior is uniformly observed, more or

less, for all the three geometries studied here; however some important distinctions will be reported in the next section. Therefore, metal nano-cavities designed for coupling spontaneous emission into lasing modes should be designed by considering their size and respective mode profiles for maximum field enhancement in the active medium.

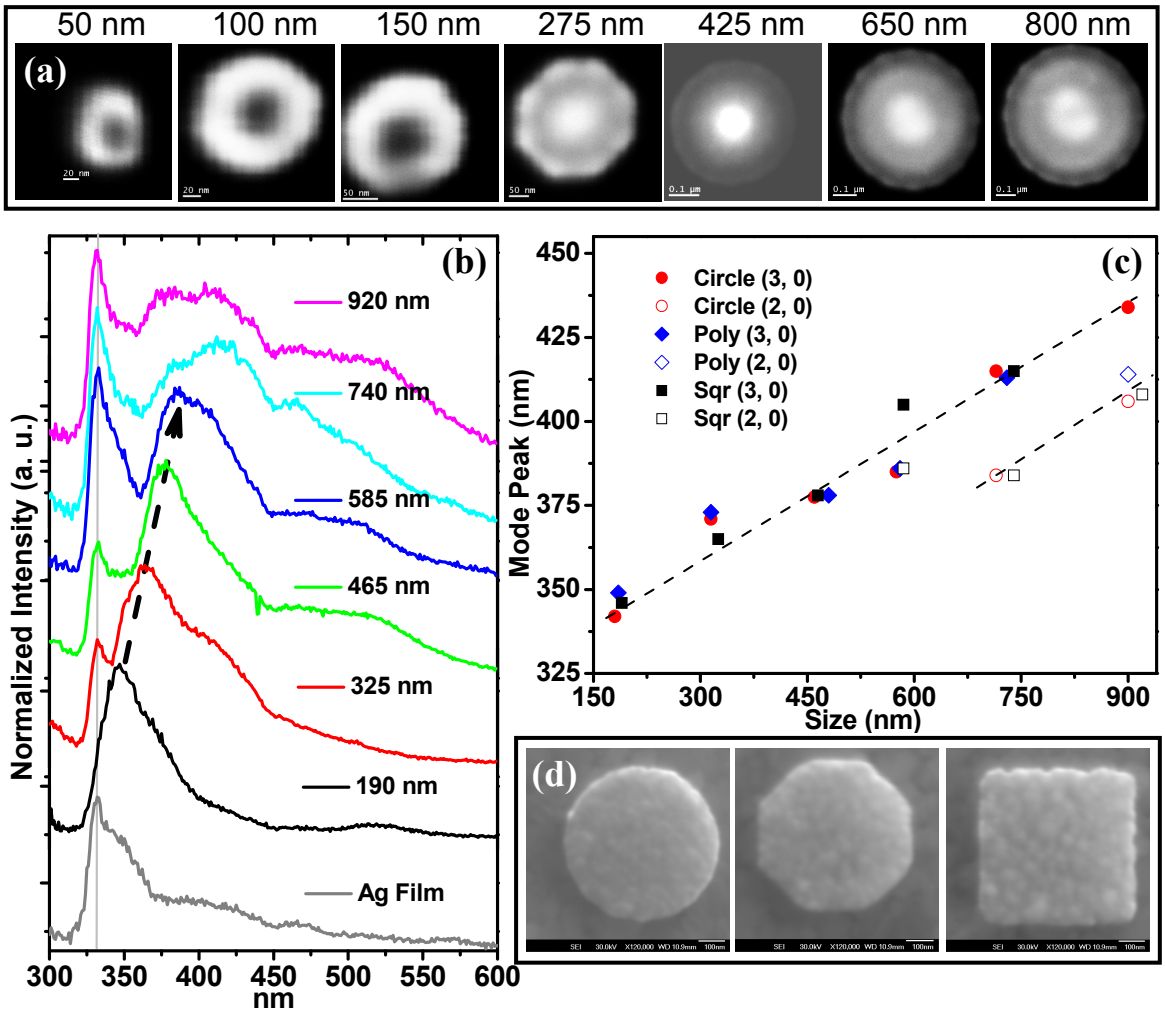

Figure 5.1: Parametric study of nano-disk modes using cathodoluminescence imaging and spectroscopy. (a) Panchromatic images of 50 nm thick Ag disks of various sizes showing different modes supported on them. (b) Spectra taken by fixing the electron-beam at the center of similar Ag disks; (c) plots of the dominant mode against disk diameter for three different geometries; (d) representative SEM images of three geometries considered here—circular, polygonal and square.

Figure 5.2 shows spectral analysis and corresponding images of various modes of a 900 nm Au disk. The spectra were taken along a line joining the center of the disk to one of the corners as shown by the numbers in the SEM image. Panchromatic images of the same disk show high luminescent corners suggesting a collage of modes with maxima at the corners and edges. The spectra show several peaks corresponding to the different modes the fixed beam is able to excite.

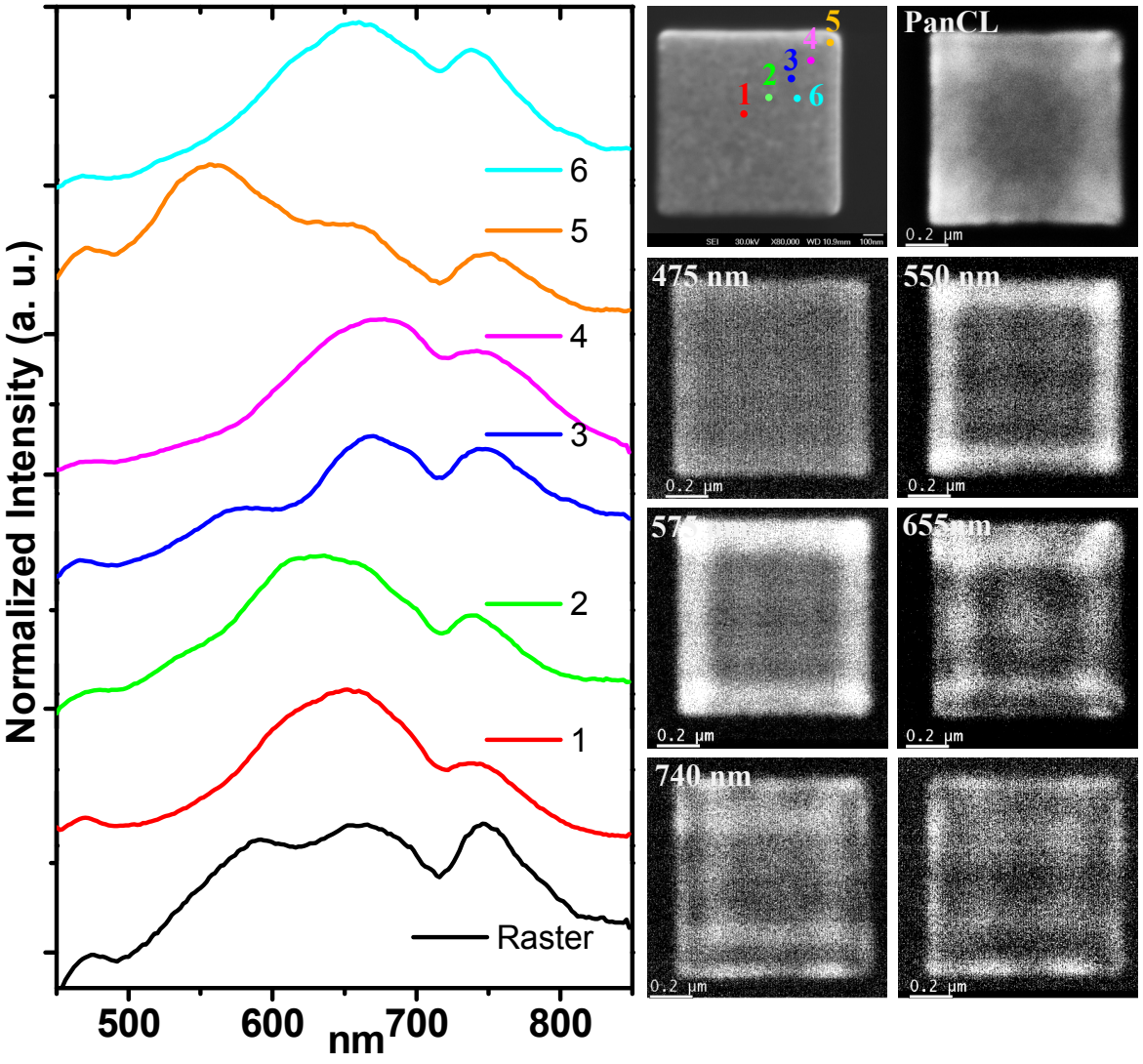

Figure 5.2: Spectral and imaging analysis of 50 nm thick Au nano-disk with 900 nm edge. The spectra collected at different positions of the disk (as numbered in SEM image) show peaks corresponding to different modes. Some of these modes are captured in the monochromatic images as shown on the right.

For smaller wavelengths, Au is very lossy [4, 79, 97, 111] and barely any charge oscillations in the monochromatic images can be observed. However, with increasing wavelengths, oscillations of the surface plasmon wave on the disk result in interference patterns in both in-plane horizontal and vertical directions [90-91]. These maxima and minima are captured as centers of high and low luminescence, respectively. Note that only modes that are multiples of half-wavelengths can be sustained. This allows calculation of SPP wavelengths for the various modes observed here; e.g., the three half-wavelengths observed at 655 nm correspond to an SPP wavelength of 640 nm while the four half-wavelengths at 550 nm correspond to 510 nm. The corresponding wavelengths calculated from dispersion relation of 50 nm thick Au film are at 620 nm and 504 nm, respectively.

5.3 Effect of disk geometry on mode splitting

In this section, the effect of geometry on plasmonic modes of a silver nano-disk is investigated. By positioning the electron-beam at specific locations of a nano-disk, completely different modes can be excited that are strongly dependent on disk-geometry. Panchromatic imaging of a circular disk shows strong luminescence at the center; however, as the disk "circularity" is modified from circular to octagonal, new modes at the periphery are observed. Investigations of octagonal disks reveal the appearance of whispering gallery-type modes attributed to splitting of degeneracy. For a square disk, a more uniform luminescence across the disk is observed suggesting weak coupling of the electron beam.

50 nm thick Ag disks with diameter of 425 nm were fabricated on 85 nm thick SiO_2 layer deposited on Si substrate as shown in Fig. 5.3. To avoid any damage to the Ag nanostructure, no RIE or wet etching was attempted as reported in the previous Chapter. This size was chosen because smaller disks prominently show TM (1,1) modes [53] with fields concentrated on the edges, making the current observations much more difficult to separate; for larger disks, more modes start to appear, resulting in a much more complicated system. Detailed analysis of modes on this disk shows that a beam focused at the center of the disk excites whispering gallery type modes which are strongly dependent on the disk geometry.

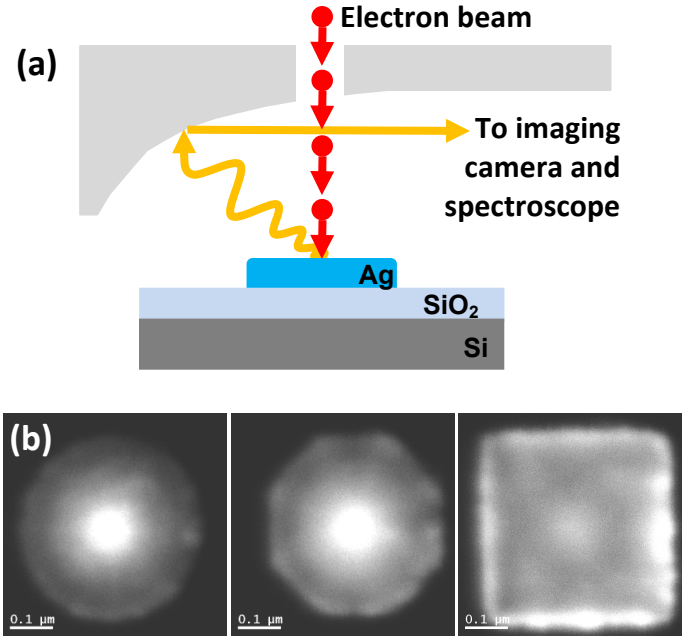

Figure 5.3: (a) Schematic of the sample design and cathodoluminescence setup. (b) Panchromatic images of the nano-disks compared for studying role of geometry on disk modes. The circular disk shows a prominently luminescent center while the octagonal disk also shows enhanced periphery suggesting appearance of new modes as the "circularity" of the disk is modified. The square disk has a weakly luminescent center but more uniform emission.

Figure 5.3 (b) shows panchromatic CL images of three disks with characteristic dimensions of 425 nm but varying "circularity"—from fully circular to a square disk. The images reveal a strong emission from the center suggesting the predominant modes to be Bessel modes of the first kind which have their maxima at center and have been studied earlier in plasmonic nano-disks [53] and micro-disk lasers [108]. The images also show that intensity at the center is strongly dependent on the geometry and lower contrast is observed as the disk changes from circular to square. While a fully circular disk shows a very strong luminescent center suggesting a predominantly single mode excitation, the square disk suggests either weak coupling with electron beam or excitation of several modes with comparable efficiency, making the whole disk uniformly luminescent. Interestingly, the octagonal disk shows increased luminescence at the periphery suggesting emergence of additional modes as imperfections are added to the periphery. In that sense, the octagonal disk appears to be a good candidate to understand how geometry affects the coupling of electron beam with a plasmonic nano-disk. This can help in understanding and designing, e.g., single mode nano-lasers with desired side-mode suppression ratio by preferably coupling light into the lasing mode.

For the purpose of understanding how change in "circularity" affects luminescence observed in panchromatic images, detailed studies of the octagonal disk were carried out. Because electron-beam allows localized excitation of the disks—in a way analogous to hitting an acoustic drum at different locations and creating unique sounds—it is worthwhile to focus the beam at several positions and investigate corresponding modes. Figure 5.4 (a) shows spectra taken by positioning the beam at different locations on the disk. When the beam is fixed at the edge or corner of disk, a

strong peak at the 345 nm is observed. This peak corresponds to the surface plasmon polariton (SPP) peak of Ag [44], and therefore suggests generation of travelling SPPs at the periphery that result in whispering gallery modes on the disk. The spectrum taken by fixing the beam at the center shows two peaks at 370 nm and 420 nm. Additionally, a beam localized at half radius from center to edge shows a predominant peak at 370 nm and a relatively weak peak at 420 nm. All the spectra also show a bulk plasmon peak of silver at 328 nm [44] and another peak of varying strength at 455 nm from the SiO_2 substrate [95]. FDTD simulations carried out using a line charge of dipoles show excellent agreement with the observed peaks.

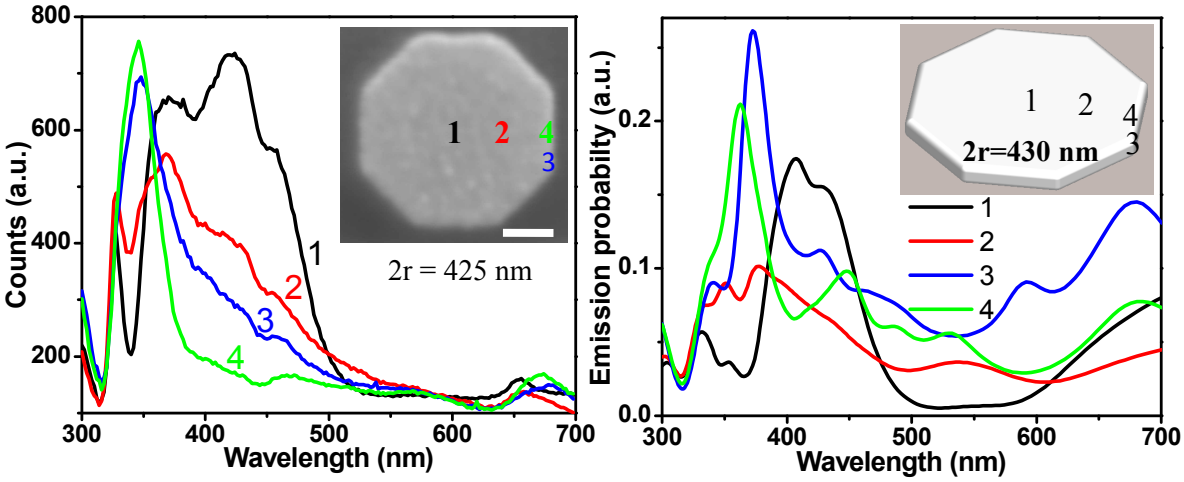

Figure 5.4: (a) Cathodoluminescence spectra taken by positioning the electron-beam at different locations on an octagonal disk of corner-to-corner diameter of 425 nm. The numbers indicate position of the beam for different spectra. Center excitation shows two peaks at 370 nm and 420 nm while excitation at half-radius predominantly excites 370 nm mode. The 455 nm peak is from SiO_2 substrate; (b) FDTD simulation confirming the experimental observation.

Because an increased luminescence is observed at the periphery when the disk is modified from circular to octagonal, any changes in the geometry should accompany excitation of new modes at the periphery, either by exciting higher Bessel modes—which

have multiple nodes away from the center—or completely different kind of modes that localize at the periphery. The first case is unlikely since the central node of higher Bessel functions should be more tightly focused to accommodate additional nodes while we observe similar (or slightly diffused) central node. To verify the second possibility, spectra taken by fixing the beam were compared, as was done for the octagonal case above. When the beam is fixed at the periphery, travelling surface plasmons of the whispering gallery modes should be expected. Their peak should remain the same although the luminescence might change depending on how efficiently they are excited. Interestingly, a comparison of spectra taken by fixing the beam at the center of the three disks showed very different behavior. For the circular and square disks, only one peak is observed instead of the two non-degenerate peaks observed for the octagonal disk.

Simulations of this observation for the three disks by fixing the electron beam in the center show splitting of the degenerate modes as the "circularity" is gradually changed (Fig. 5.5 (b)). More interestingly, the field profiles for the two modes suggest two whispering gallery (WG) type modes with different field maxima (Fig. 5.5 (c)). For the low energy mode, the field is concentrated on corners of the disk while for the higher energy mode, this field maxima lies on edges. One approach to understand the splitting is by comparing the total surface area of the two modes. When the field maxima spots are connected using a polyline, the area within the polygon of high energy edge mode is found to be smaller than the low energy mode. Therefore, the change in periphery has resulted in excitation of two different Bessel functions of different sizes. For the square case, several such modes can be sustained making the disk much more luminescent as is confirmed by the broad simulated peak. However, the single weak peak in the

experiments suggests one of these modes is much more dominant than others. Similar splitting has also been expected from edge roughness [110], and therefore other parameters that need to be considered in future for designing single mode resonant nano-cavities.

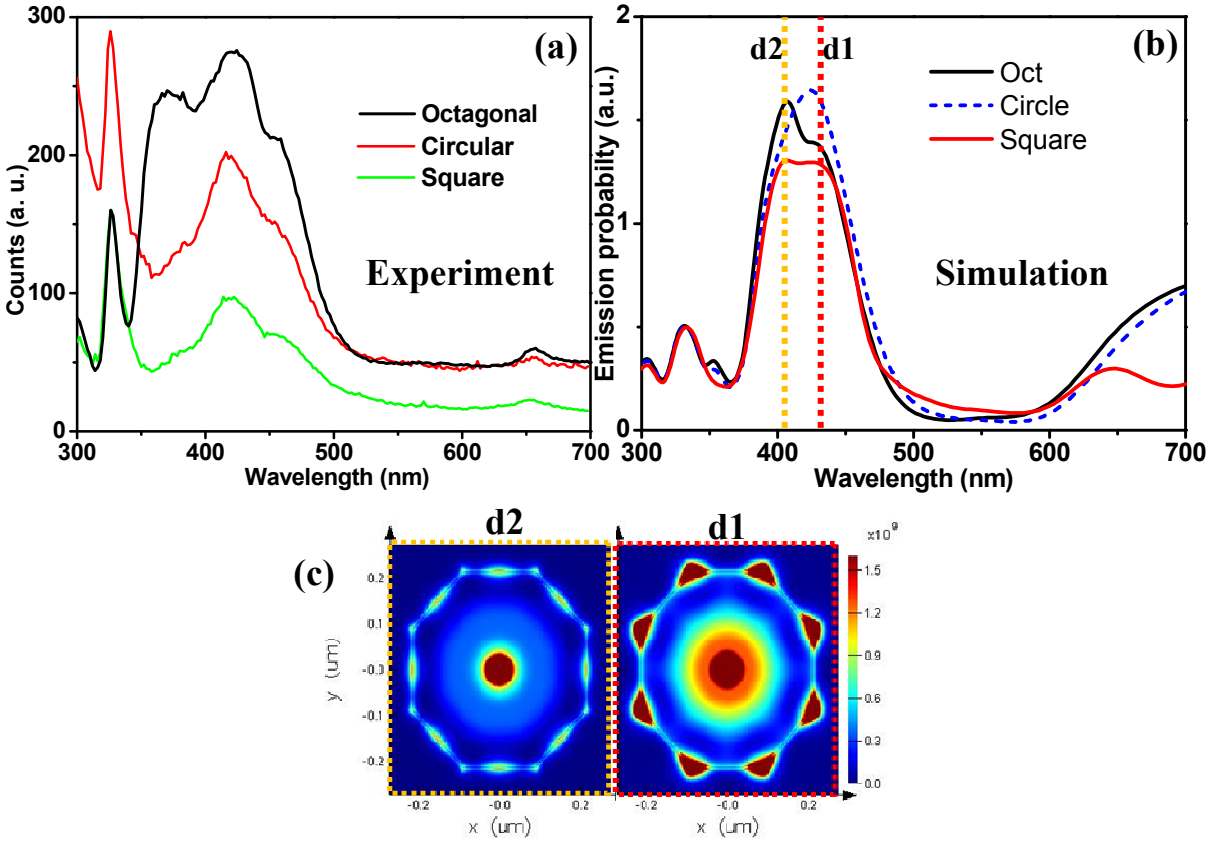

Figure 5.5: Spectra of the three disks with different geometries for excitation using electron-beam fixed at center. (a) Experimental measurements and (b) the corresponding simulations. Splitting of degeneracy is clearly captured in simulations as the disk "circularity" changes. (c) Electric field patterns for octagonal disk at the two peaks show different spatial field distribution with maxima at corners (d1) and edges (d2).

5.4 Summary

Cathodoluminescence imaging and spectroscopy allows mapping of different modes of plasmonic nano-disks that are comparable in size with their resonance

wavelengths. Investigations using panchromatic images as well as spectral analysis suggest small disks are good candidates for single mode resonances; however, as the disk size increases more modes are observed. Monochromatic images of these modes showed they are strongly dependent on their size as well as the location of the excitation source. The strong dependence of geometry is characterized using three disks with circular, octagonal and square shapes. When a circular disk is modified to octagonal, splitting of the peak for center excited mode was observed. The perturbation created at the edges results in two separate whispering gallery-type modes that have different SPP path lengths showing field maxima at corners and edges. Therefore, imperfections resulting from fabrication (edge roughness, roundness, etc.) of plasmonic devices can have important implications on next generation plasmonic applications (e.g., lasing cavities) and should be included during characterization.

CHAPTER 6

SUMMARY AND FUTURE OUTLOOK

6.1 Summary

This thesis discusses various aspects related to the study of optical nano-antennas. Because of their nanoscale size, both fabrication and characterization of optical antennas offer significant challenges for harnessing their unique properties for a wide range of applications. Therefore, a broader approach involving patterning, characterization and applications is taken. This should enable future studies of optical antennas by providing fundamental understanding of their behavior as well as simple methods of manufacturing them.

Chapter 1 introduces the concept of optical nano-antenna and how extension of antenna theory from radio-frequency alone may not be sufficient to understand their optical counterpart. The great strides made over the last decade in understanding their behavior as well as the wide range of applications reported so far are discussed. A broad range of techniques are employed in understanding their fundamental properties using plane-wave as well as electron-beam sources. This chapter also gives a brief outline of the thesis and various aspects that are to be addressed in remaining Chapters.

One of the main reasons behind the recent surge in research in optical antennas is the progress made in fabricating sub-100 nm features. Chapter 2 discusses various aspects of design and fabrication. Electron-beam lithography is the most important tool for patterning at this scale and was optimized for the studies here. However, due to high cost and complexity involved in the process, there is a strong desire to search for

alternative methods to fabricate these nanostructures. A newly developed technique involving direct metal patterning using a solid ionic conductor is introduced in this chapter, which holds promise for sub-10 nm feature patterning over several millimeters. New ways to enhance the capability of this technique are discussed, with special emphasis given to the mechanical characterization of the superionic stamp used for etching the metal. Different ways to improve the metal film quality as well as the role of deformation of the ionic conductor in etching are discussed.

Two approaches to antenna characterization are discussed. Chapter 3 outlines the first approach that involves investigation of various aspects of the antenna behavior using an optical source. The role of antenna geometry as well as the nature of the excitation source in the antenna behavior is discussed. Arrays of bowties were identified as possible candidates for applications in non-linear spectroscopy. Irradiation using a high-power pulsed laser resulted in a rich source of non-linear signal and several processes of sum-frequency generation were identified. High electromagnetic fields from the antennas were identified as a possible source of these non-linear processes and found to be promising for the next generation of optical devices.

While optical excitation is the most commonly used methodology for studying optical resonators, it is limited in terms of resolution as well as excitation of higher modes. In this regard, electron-beam excitation offers several unique opportunities including capability of sub-Å resolution, matching with a broad range of wave-vectors, and ability to excite “dark” modes that do not readily couple with optical sources and show high quality factors than normally observed for the “bright” modes. Chapter 4 discusses application of one such technique called cathodoluminescence (CL) imaging

spectroscopy for mapping various modes of triangles and bowtie antennas. Several modes are identified by localizing the electron beam near the hotspots of triangles. Additionally, "bright" and "dark" modes of the hybridized bowties were characterized. Finite difference time domain simulations were used to confirm the experimental observations.

Using the new capability to map dark modes of nano-antennas, Chapter 5 investigates the highly localized ultrasmall modes of nano-disks which are a new class of resonators with characteristic dimensions comparable to their resonance wavelengths. Their large sizes result in several modes that are spatially and spectrally resolved using localized excitations. As an example of how CL allows mapping of important properties of the resonators, the effect of disk geometry on mode splitting was discussed.

6.2 Future work

The work presented here has strongly emphasized on fabrication and characterization, allowing possibilities of new applications based on the understanding gained so far. From the fabrication perspective there are a few aspects that can help further improve the capability of the currently reported process:

- Embossing based S4 process should be explored to pattern even smaller features with the possibility of sub-5 nm features. The smallest reported features here are the bowtie gaps; however, it will be interesting to see what sizes of dots and lines can be fabricated using this approach. Currently, fabrication of sub-50 nm thin lines is a major challenge and overcoming the barriers will require not only more understanding of the etching process but also further improvement in metal film quality.

- While proof-of-concept experiments are shown to demonstrate the ability to scale up the embossing based S4 process, the true capability has been limited by inability to make large templates and emboss them over large areas. The first issue can be addressed using nano-imprint lithography, which has made it much more affordable to make large area patterns. However, the engineering challenges associated with embossing such a large template onto Ag_2S or other non-polymeric stamps will require state-of-the-art techniques.
- This thesis has mainly discussed Ag_2S as a possible candidate for fabricating small features required for optical frequency resonators. However, a wide range of ionic conductors exist and need to be explored.
- The bulk deformation of ionic stamps was shown to dramatically enhance the etching process. Further work is required for fundamental understanding of process and how it can be better harnessed for important applications, e.g., ionic actuation, battery technology, and metal intercalation.
- The current approach of film quality improvement using thin MgO buffer layer underneath silver films was inspired by the fact that the Ag-MgO lattice constants show very small mismatch. However, NiO has even smaller mismatch and further investigations are required to understand the role of NiO buffer layers. An important challenge that needs to be addressed is the tendency of NiO to dissociate during deposition.

From the perspective of characterization and applications of antennas, current studies can further help in several important ways. However, more work needs to be done to make them useful for mainstream applications:

- While linear behavior of optical nano-antennas has been widely reported and well understood, their role in non-linear processes is still largely unexplored. One important implication will be in harnessing the solar spectrum below Si band-gap which accounts for about one-third of total solar energy.
- A clear understanding of the role played by the linear enhancement in the non-linear signal is still lacking. This will allow better antenna design for non-linear spectroscopy and can help in developing resonators for and beyond ultra-violet without having to deal significantly with high losses in metals at these frequencies.
- Not only will the capability to simulate the non-linear behavior be a great boost for optical antennas but it will also revolutionize several fields. However, it requires fundamental breakthroughs including understanding of the non-linear behavior of materials and ability to incorporate them in current modeling packages.
- The theoretical resolution of cathodoluminescence is several orders of magnitude better than the currently best known resolution of ~20 nm. Better sample designs, improved monochromators on current CL setup, and new approaches, e.g., similar to superlensing in optical characterizations can help in improving the current resolution limit.

- This thesis has mostly focused on antenna characterization, using cathodoluminescence; however, knowledge gained from mapping the different modes of optical antennas needs to be utilized for other applications.
- Additionally, the understanding gained from mapping of nano-disk modes can help design better cavity resonators. Current active devices, e.g., nano-lasers, can help in maximizing the overlapping of mode profile with the active region of the lasing cavity. Moreover, these studies can help in better coupling of the spontaneous emission and enhanced Purcell factor.

6.3 Outlook

Optical antennas are promising devices for the next generation of applications, e.g., all optical communication and thresholdless nano-lasers. They are also important for understanding interaction of light with matter at the nanoscale. Therefore, recent progress made in understanding optical antennas over the last decade is highly encouraging. The exponential growth in the number of high-impact publications also promises to sustain the progress.

However, future growth requires a more holistic approach involving both materials as well as optical aspects of the research. Better ways to manufacture various antenna designs with ever smaller features is one of the critical aspects that need to be addressed. This requires sustained effort both in terms of understanding the material properties as well as engineering of methodologies that can help pattern features at this scale. Nano-imprint lithography has made great strides in recent years with the capability

to pattern sub-20 nm half line-widths over large areas and its incorporation into the S4 process offers great opportunities for patterning the next generation of optical resonators.

Understanding the nature of resonance using cathodoluminescence and optical characterization is only the first step in their application in critical areas of future devices. The theoretically predicted sub-Å resolution using electron-beam characterization tools is still several orders away; however, it has already helped in understanding some critical aspects of antennas.

The application of optical antennas in sensing is one of the most sought-after goals of research. Enhancing the signal in surface-enhanced Raman spectroscopy (SERS) can help in designing table-top systems with below nano-molar sensitivity. Recent enhancement factors above 10^{11} [24] suggest mainstream application may not be far away. Similarly, fluorescence sensing of single molecules can benefit from the high electromagnetic fields of antennas. One of the most important milestones in application of optical antennas will be the arrival of Seagate's latest hard disk drive that is expected to hit the market in 2013. It will utilize the quadrupole mode of a 70 nm gold sphere for heat-assisted magnetic recording [28].

APPENDIX A

DARK AND BRIGHT MODES OF 75 nm BOWTIE

A.1 Modes of 75 nm bowtie

In Chapter 4, bright and dark modes of 110 nm bowties were reported. Because dark modes have been mapped for the first time using photon collection in an electron-beam based technique, further investigations on other bowties were carried out to confirm this observation. Figure A.1 shows the experimentally observed spectra of the three modes for a 75 nm bowtie with 8 nm gap.

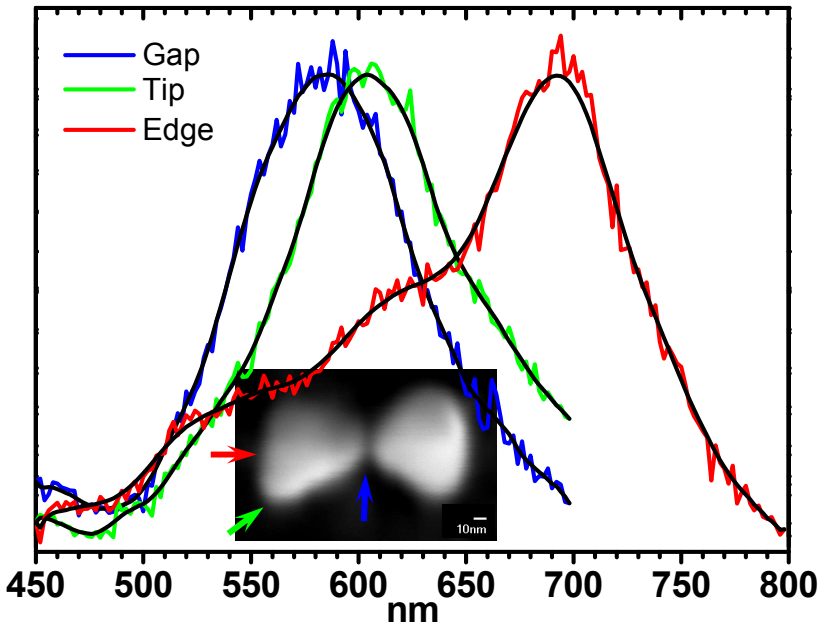

Figure A.1: Spectra taken by localizing the electron-beam in the gap (blue) and near tip (green) and edge (red) of a bowtie with triangle edge-to-tip length of 75 nm and 8 nm gap. The beam in gap excites anti-parallel (dark) while the other two are parallel (bright) modes. The arrows in inset image show the location of the electron-beam.

Figure A.2 reports the simulated spectra for this size bowtie and shows excellent agreement with the experimental peaks for the dark and bright modes.

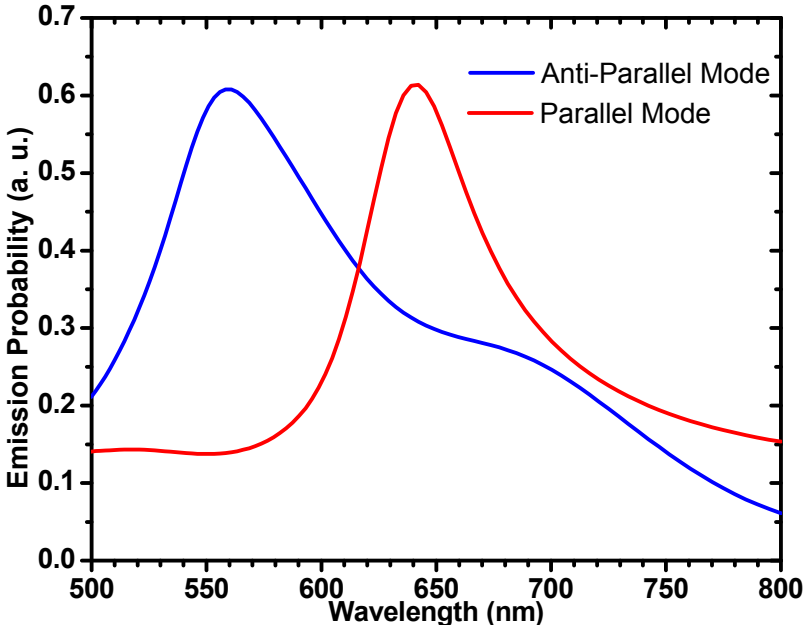

Figure A.2: Simulated anti-parallel (dark) and parallel (bright) mode spectra of the 75 nm bowtie with 5 nm gap.

REFERENCES

[1] N. J. Halas, "Connecting the dots: Reinventing optics for nanoscale dimensions," PNAS **106** (10), 3643 (2009).

[2] L. Novotny and N. van Hulst, "Antennas for light," Nature Photon. **5**, 83 (2011).

[3] P. Mühlschlegel, H.-J. Eisler, O. J. F. Martin, B. Hecht, and D. W. Pohl, "Resonant optical antennas," Science **308**, 1607 (2005).

[4] K. B. Crozier, A. Sundaramurthy, G. S. Kino, and C. F. Quote, "Optical antennas: Resonators for local field enhancement," J. Appl. Phys. **94** (7), 4632 (2003).

[5] L. Novotny, "Effective wavelength scaling for optical antennas," Phys. Rev. Lett. **98**, 266802 (2007).

[6] G. W. Bryant, F. J. García de Abajo, and J. Aizpurua, "Mapping the plasmon resonances of metallic nanoantennas," Nano Lett. **8** (2), 601 (2008).

[7] W. L. Barnes, A. Dereux, and T. W. Ebbesen, "Surface plasmon subwavelength optics," Nature **424**, 824 (2003).

[8] A. Sundaramurthy, K. B. Crozier, and G. S. Kino, "Field enhancement and gap-dependent resonance in a system of two opposing tip-to-tip Au nanotriangles," Phys. Rev. B **72**, 165409 (2005).

[9] E. Ozbay, "Plasmonics: merging photonics and electronics at nanoscale dimensions," Science **311**, 189 (2006).

[10] A. Alù and N. Engheta, "Input impedance, nanocircuit loading, and radiation tuning of optical nanoantennas," Phys. Rev. Lett. **101**, 043901 (2008).

[11] N. Engheta, A. Salandrino, and A. Alù, "Circuit elements at optical frequencies: Nanoinductors, nanocapacitors, and nanoresistors," Phys. Rev. Lett. **95**, 095504 (2005).

[12] J.-J. Greffet, M. Laroche, and F. Marquier, "Impedance of a nanoantenna and a single quantum emitter," Phys. Rev. Lett. **105**, 117701 (2010).

[13] M. Brongersma, "Engineering optical nanoantennas," Nature Photon. **2**, 270 (2008).

[14] J. H. Kang, D. S. Kim, and Q-Han Park, "Local capacitor model for plasmonic electric field enhancement," Phys. Rev. Lett. **102**, 093906 (2009).

[15] T. Zentgraf, T. P. Meyrath, A. Seidel, S. Kaiser, H. Giessen, C. Rockstuhl, and F. Lederer, "Babinet's principle for optical frequency metamaterials and nanoantennas," Phys. Rev. B **76**, 033407 (2007).

[16] J.-S. Huang, T. Feichtner, P. Biagioni, and B. Hecht, "Impedance matching and emission properties of nanoantennas in an optical nanocircuit," Nano Lett. **9** (5), 1897 (2009).

[17] J. Li, A. Salandrino, and N. Engheta, "Shaping light beams in the nanometer scale: A Yagi-Uda nanoantenna in the optical domain," Phys. Rev. B **76**, 245403 (2007).

[18] K. L. Kelly, E. Coronado, L. L. Zhao, and G. C. Schatz, "The optical properties of metal nanoparticles: The influence of size, shape, and dielectric environment," J. Phys. Chem. B **107**, 668 (2003).

[19] B. Baumeier, T. A. Leskova, and A. A. Maradudin, "Cloaking from surface plasmon polaritons by a circular array of point scatters," Phys. Rev. Lett. **103**, 246803 (2009).

[20] S. Kim, J. Jin, Y.-J. Kim, I.-Y. Park, Y. Kim, and S.-W. Kim, "High-harmonic generation by resonant plasmon field enhancement," Nature **453**, 757 (2008).

[21] T. H. Taminiau, F. D. Stefani, F. B. Segerink, and N. F. van Hulst, "Optical antennas direct single-molecule emission," Nature Photon. **2**, 234 (2008).

[22] S. Kühn, U. Håkanson, L. Rogobete, and V. Sandoghdar, "Enhancement of single-molecule fluorescence using a gold nanoparticles as an optical nanoantenna," Phys. Rev. Lett. **97**, 017402 (2006).

[23] A. Kinkhabwala, Z. Yu, S. Fan, Y. Avlasevich, K. Müllen, and W. E. Moerner, "Large single-molecule fluorescence enhancements produced by a bowtie nanoantenna," Nature Photon. **3**, 654 (2009).

[24] N. A. Hatab, C.-H. Hsueh, A. L. Gaddis, S. T. Retterer, J.-H. Li, G. Eres, Z. Zhang, and B. Gu, "Free-standing optical gold bowtie nanoantenna with variable gap size for enhanced Raman spectroscopy," Nano Lett. **10** (12), 4952 (2010).

[25] A. Sundaramurthy, P. J. Schuck, N. R. Conley, D. P. Fromm, G. S. Kino, and W. E. Moerner, "Toward nanometer-scale optical photolithography: utilizing the near-field of bowtie optical nanoantennas," Nano Lett. **6** (3), 355 (2006).

[26] T. Xu, Y.-K. Wu, X. Luo, and L. J. Guo, "Plasmonic nanoresonators for high-resolution colour filtering and spectral imaging," Nature Comm. **1**, 59 (2010).

[27] H. A. Atwater and A. Polman, "Plasmonics for improved photovoltaic devices," Nature Mater. **9**, 205 (2010).

[28] W. A. Challener, C. Peng, A. V. Itagi, D. Karns, W. Peng, Y. Peng, X.-M. Yang, X. Zhu, N. J. Gokemeijer, Y.-T. Hsia, G. Ju, R. E. Rottmayer, M. A. Seigler, and E. C. Gage "Heat-assisted magnetic recording by a near-field transducer with efficient optical energy transfer," Nature Photon. **3**, 220 (2009).

[29] A. G. Curto, G. Volpe, T. H. Taminiau, M. P. Kreuzer, R. Quidant, and N. F. van Hulst, "Unidirectional emission of a quantum dot coupled to a nanoantenna," Science **329**, 930 (2010).

[30] K. Ko, A. Kumar, K. H. Fung, R. Ambekar, G. L. Liu, N. X. Fang, and K. C. Toussaint, Jr., "Nonlinear optical response from arrays of Au bowtie nanoantennas," Nano Lett. **11** (1), 61 (2011).

[31] W. Rechberger, A. Hohenau, A. Leitner, J. R. Krenn, B. Lamprecht, and F. R. Aussenegg, "Optical properties of two interacting gold nanoparticles," Opt. Comm. **220**, 137 (2003).

[32] J. Merlein, M. Kahl, A. Zuschlag, A. Sell, A. Halm, J. Boneberg, P. Leiderer, A. Leitenstorfer, and R. Bratschitsch, "Nanomechanical control of an optical antenna," Nature Photon. **2**, 230 (2008).

[33] E. Hao and G. C. Schatz, "Electromagnetic fields around silver nanoparticles and dimers," J. Chem. Phys. **120** (1), 357 (2004).

[34] D. P. Fromm, A. Sundaramurthy, P. James Schuck, G. Kino, and W. E. Moerner, "Gap-dependent optical coupling of single bowtie nanoantennas resonant in the visible," Nano Lett. **4** (5), 957 (2005).

[35] P. J. Schuck, D. P. Fromm, A. Sundaramurthy, G. S. Kino, and W. E. Moerner, "Improving the mismatch between light and nanoscale objects with gold bowtie nanoantennas," Phys. Rev. Lett. **94**, 017402 (2005).

[36] P. Biagioni, J. S. Huang, L. Duò, M. Finnazi, and B. Hecht, "Cross-resonant optical antenna," Phys. Rev. Lett. **102**, 256801 (2009).

[37] Z. Zhang, A. Weber-Bargioni, S. W. Wu, S. Dhuey, S. Cabrini, and P. J. Schuck, "Manipulating nanoscale light fields with the asymmetric bowtie nano-colorsorter," Nano Lett. **9** (12), 4505 (2009).

[38] R. Vogelgesang and A. Dmitriev, "Real-space imaging of nanoplasmonic resonances," Analyst **135**, 1175 (2010).

[39] J. Xu, A. Kumar, P. Chaturvedi, K. H. Hsu, and N. X. Fang, "Enhancing light coupling with plasmonic optical antennas," in *Metamaterials: Theory, Design, and Applications*, edited by T. J. Cui, D. Smith, and R. Liu (Springer, NY, 2010).

[40] M. Schnell, A. García-Etxarri, A. J. Huber, K. Crozier, J. Aizpurua, and R. Hillenbrand, "Controlling the near-field oscillations of loaded plasmonic nanoantennas," Nature Photon. **3**, 287 (2009).

[41] R. D. Grober, R. J. Schoelkopf, and D. E. Prober, "Optical antenna: Towards a unity efficiency near-field optical probe," Appl. Phys. Lett. **70** (11), 1354 (1997).

[42] F. J. Garcia de Abajo, "Optical excitations in electron microscopy," Rev. Mod. Phys. **82**, 209 (2010).

[43] J. Nelayah, M. Kociak, O. Stéphan, F. Garcia de Abajo, M. Tencé, L. Henrard, D. Taverna, I. Pastoriza-Santos, L. M. Liz-Marzán, and C. Colliex, "Mapping surface plasmon on a single metallic nanoparticles," Nature Physics **3**, 348 (2007).

[44] M. Kuttge, "Cathodoluminescence plasmon microscopy," Ph.D. dissertation, Utrecht University, 2009.

[45] P. Chaturvedi, K. H. Hsu, A. Kumar, K. H. Fung, J. C. Mabon, and N. X. Fang, "Imaging of plasmonic modes of silver nanoparticles using high-resolution cathodoluminescence spectroscopy," ACS Nano **3**, 2965 (2009).

[46] A. Kumar, K.-H. Fung, J. C. Mabon, E. Chow, and N. X. Fang, "Excitation and imaging of resonant optical modes of Au triangular nanoantennas using cathodoluminescence spectroscopy," J. Vac. Sci. Technol. B **28**, C6C21 (2010); http://arxiv.org/pdf/1010.0057.

[47] K. H. Hsu, P. L. Schultz, P. M. Ferreira, and N. X. Fang, "Electrochemical nanoimprinting with solid-state superionic stamp," Nano Lett. **7** (2), 446 (2007).

[48] P. L. Schultz, K. H. Hsu, N. X. Fang, and P. M. Ferreira, "Solid-state electrochemical nanoimprinting of copper," J. Vac. Sci. Technol. B **25** (6), 2419 (2007).

[49] A. Kumar, K. H. Hsu, K. E. Jacobs, P. M. Ferreira, and N. X. Fang, "Direct metal nano-imprinting using embossed solid electrolyte stamp," Nanotechnology **22**, 155302 (2011); http://arXiv.org/abs/1102.1945.

[50] K. H. Hsu, P. L. Schultz, P. M. Ferreira, and N. X. Fang, "Exploiting transport of guest metal ions in a host ionic crystal lattice for nanofabrication: Cu nanopatterning with Ag_2S," Appl. Phys. A **97** (4), 863 (2009).

[51] A. Kumar, K. H. Fung, and N. X. Fang, "Probing surface-plasmon hybridization using cathodoluminescence" (to be published).

[52] A. Kumar, K. H. Fung, and N. X. Fang, "Mapping of surface plasmon polaritons on nanostructured thin film disks using cathodoluminescence imaging," Proc. SPIE **7946**, 79461U (2011); doi:10.1117/12.875881.

[53] M. Kuttge, F. J. García de Abajo, and A. Polman, "Ultrasmall mode volume plasmonic nanodisk resonators," Nano Lett. **10**, 1437 (2009).

[54] E. Prodan, C. Radloff, N. J. Halas, P. Nordlander, "A hybridization model for the plasmon response of complex nanostructures," Science **302**, 419 (2003).

[55] A. Kumar, K. H. Hsu, K. E. Jacobs, P. M. Ferreira, and N. X. Fang, "Direct metal nano-patterning using embossed solid electrolyte stamp," Mat. Res. Soc. Symp. Proc. **1156**, 141 (2009).

[56] A. Kumar, K. H. Hsu, P. Chaturvedi, H. Ma, J. Xu, and N. X. Fang, "Fabrication and optical characterization of bowtie antennas," IEEE Conf., Nanotechnology (NANO '08, Arlington, TX, 2008), pp. 98-99.

[57] A. Kumar, K. Hsu, K. Jacobs, P. Ferreira, and N. Fang, "Characterizing the role of deformation during electrochemical etching of metallic films," Mar. Res. Soc. (MRS Fall 2010, Boston, MA).

[58] Y. Huang, W. Zhou, K. J. Hsia, E. Menard, J.-U. Park, J. A. Rogers, and A. G. Alleyne, "Stamp collapse in soft lithography," Langmuir **21** (7), 8058 (2005).

[59] C. Wagner, "Investigations on silver sulfide," J. Chem. Phys. **21**, 1819 (1953).

[60] R. L. Allen and W. J. Moore, "Diffusion of silver in silver sulfide," J. Phys. Chem. **63**, 223 (1959).

[61] V. J. Logeeswaran, N. P. Kobayashi, M. S. Islam, W. Wu, P. Chaturvedi, N. X. Fang, S. Y. Wang, and R. S. Williams, "Ultra-smooth silver thin films deposited with a germanium nucleation layer," Nano Lett. **9** (1), 178 (2009).

[62] V.A. Heinrich and P.A. Cox, *The Surface Science of Metal Oxides* (Cambridge University Press, Cambridge, UK, 1996).

[63] S. Schintke, S. Messerli, M. Pivetta, F. Patthey, L. Libioulle, M. Stengel, A. De Vita, and W. D. Schneider, "Insulator at the ultrathin limit: MgO on Ag(001)," Phys. Rev. Lett. **87**, 276801 (2001).

[64] O. Rabach, G. Renaud, and A. Barbier, "Structure and morphology of the Ag/MgO(001) interface during in situ growth at room temperature," Phys. Rev. B **60** (8), 5858 (1999).

[65] D. Fuks, S. Dorfman, Y. F. Zhukovskii, E. A. Kotomin, and A. M. Stoneham, "Theory of the growth mode for a thin metallic film on an insulating substrate," Surf. Sci. **499**, 29 (2002).

[66] X. Y. Chen, B. Yang, Z. G. Liu, and L. J. Shi, "Growth of completely (110)- and (111)-oriented MgO films on H-terminated 100 silicon substrate by pulsed laser deposition," Appl. Surf. Sci. **135**, 233 (1998).

[67] M. Ning, Y. Y. Mi, C. K. Ong, P. C. Lim, and S. J. Wang, "Growth studies of (220), (200) and (111) oriented MgO films on Si(001) without buffer layer," J. Phys. D **40**, 3678 (2007).

[68] C. Li, R. Wu, A. J. Freeman, and C. L. Fu, "Energetics, bonding mechanism, and electronic structure of metal-ceramic interfaces: Ag/MgO(001)," Phys. Rev. B **48**, 8317 (1993).

[69] C. Sönnichsen, T. Franzl, T. Wilk, G. von Plessen, J. Feldmann, O. Wilson, and P. Mulvaney, "Drastic reduction of plasmon damping in gold nanorods," Phys. Rev. Lett. **88**, 077402 (2002).

[70] C. Dahmen, B. Schmidt, and G. von Plessen, "Radiation damping in metal nanoparticle pairs," Nano Lett. **7** (2), 318 (2007).

[71] K. H. Hsu, J. H. Back, K. H. Fung, P. M. Ferreira, M. Shim, and N. X. Fang, "SERS EM field enhancement study through fast Raman mapping of Sierpinski carpet arrays," J. Raman Spectrosc. **41** (10), 1124 (2010).

[72] B. T. Draine and P. J. Flatau, "User guide for the Discrete Dipole Approximation Code DDSCAT 7.0," http://arxiv.org/abs/0809.0337.

[73] C. F. Bohren and D. R. Huffman, in *Absorption and Scattering of Light by Small Particles* (John Wiley, New York, NY, 1983).

[74] K. H. Fung, P. Chaturvedi, A. Kumar, K. H. Hsu, and N. X. Fang, "Far field and near field properties of triangular metal nanoparticle and nanopatterns of 3-fold rotational symmetry," in *Advances in Optical Materials*, OSA Technical Digest (CD) (Optical Society of America, 2009), paper AThA5.

[75] B. Auguire and W. L. Barnes, "Collective resonances in gold nanoparticles arrays," Phys. Rev. Lett. **101**, 143902 (2008).

[76] V. G. Kravets, F. Schedin, and A. N. Grigorenko, "Extremely narrow plasmon resonances based on diffraction coupling of localized plasmons in arrays of metallic nanoparticles," Phys. Rev. Lett. **101**, 087403 (2008).

[77] V. A. Markel, "Divergence of dipole sums and the nature of non-Lorentzian exponentially narrow resonances in one-dimensional periodic arrays of nanospheres," J. Phys. B: At. Mol. Opt. Phys. **38**, L115 (2005).

[78] T. Hanke, G. Krauss, D. Trautlein, B. Wild, R. Bratschitsch, and A. Leitenstorfer, "Efficient nonlinear light emission of single gold optical antennas driven by few-cycle near-infrared pulses," Phys. Rev. Lett. **103**, 257404 (2009).

[79] M. T. Hill, Y.-S. Oei, B. Smalbrugge, Y. Zhu, T. de Vries, P. J. van Veldhoven, F. W. M. van Otten, T. J. Eijkemans, J. P. Turkiewicz, H. de Waardt, E. J. Geluk, S.-H. Kwon, Y.-H. Lee, R. Notzel, and M. K. Smit, "Lasing in metallic-coated nanocavities," Nature Photon. **1**, 589 (2007).

[80] R. F. Oulton, V. J. Sorger, T. Zentgraf, R.-M. Ma, C. Gladden, L. Dai, G. Bartal, and X. Zhang, "Plasmon lasers at deep subwavelength scale," Nature **461**, 629 (2009).

[81] R. F. Oulton, V. J. Sorger, D. A. Genov, D. F. P. Pile and X. Zhang, "A hybrid plasmonic waveguide for subwavelength confinement and long-range propagation," Nature Photon. **2**, 496 (2008).

[82] L. Novotny and B. Hecht, *Principles of Nano-Optics* (Cambridge University Press, Cambridge, UK, 2006).

[83] J. Nelayah, M. Kociak, O. Stéphan, N. Geuquet, L. Henrard, F. J. García de Abajo, I. Pastoriza-Santos, L. M. Liz-Marzán, and C. Colliex, "Two-dimensional quasistatic stationary short range surface plasmons in flat nanoprisms," Nano Lett. **10**, 902 (2010).

[84] A. L. Koh, K. Bao, I. Khan, W. E. Smith, G. Kothleitner, P. Nordlander, S. A. Maier, and D. W. McComb, "Electron energy-loss spectroscopy (EELS) of surface plasmons in single silver nanoparticles and dimers: Influence of beam damage and mapping of dark modes," ACS Nano **3** (10), 3015 (2009).

[85] A. L. Koh, A. I. Fernández-Domínguez, D. W. McComb, S. A. Maier, and J. K. W. Yang, "High-resolution mapping of electron-beam-excited plasmon modes in lithographically defined gold nanostructures," Nano Lett. **11**, 1323 (2011).

[86] N. Yamamoto, K. Araya, and F. J. García de Abajo, "Photon emission from silver particles induced by a high-energy electron beam," Phys. Rev. B **64**, 205419 (2001).

[87] N. Yamamoto, M. Nakano, and T. Suzuki, "Light emission by surface plasmons on nanostructures of metal surfaces induced by high-energy electron beam," Surf. Interface Anal. **38**, 1725 (2006).

[88] E. J. R. Vesseur, R. de Waele, M. Kuttge, and A. Polman, "Direct observation of plamonic modes in Au nanowires using high-resolution cathodoluminescence spectroscopy," Nano Lett. **7** (9), 2843 (2007).

[89] M. Kuttge, W. Cai, F. J. García de Abajo, and A. Polman, "Dispersion of metal-insulator-metal plasmon polaritons probed by cathodoluminescence imaging spectroscopy," Phys. Rev. B **80**, 033409 (2009).

[90] X. L. Zhu, Y. Ma, J. S. Zhang, J. Xu, X. F. Wu, Y. Zhang, X. B. Han, Q. Fu, Z.M. Liao, L. Chen, and D. P. Yu, "Confined three-dimensional plasmon modes inside a ring-shaped nanocavity on a silver film imaged by cathodoluminescence microscopy," Phys. Rev. Lett. **105**, 127402 (2010).

[91] X. Zhu, Y. Zhang, J. Zhang, J. Xu, Y. Ma, Z. Li, and D. Yu, "Ultrafine and smooth full metal nanostructures for plasmonics," Adv. Mater. **22**, 4345 (2010).

[92] C. E. Hofmann, E. J. R. Vesseur, L. A. Sweatlock, H. J. Lezec, F. J. García de Abajo, A. Polman, and H. A. Atwater, "Plasmonic modes of annular nanoresonators imaged by spectrally-resolved cathodoluminescence," Nano Lett. **7**, 3612 (2007).

[93] E. J. R. Vesseur, F. J. García de Abajo, and A. Polman, "Modal decomposition of surface-plasmon whispering gallery resonators," Nano Lett. **9**, 3147 (2009).

[94] P. D. Townsend, T. Karali, A. P. Rowlands, V. A. Smith, and G. Vazquez, "Recent examples of cathodoluminescence as a probe of surface structure and composition," Mineral Mag. **63**, 211 (1999).

[95] X. Liu, J. C. H. Phang, D. S. H. Chan, and W. K. Kim, "The properties of 2.7 eV cathodoluminescence from SiO_2 films on Si substrate," J. Phys. D: Appl. Phys. **32**, 1563 (1999).

[96] M.-W. Chu, V. Myroshnychenko, C. H. Chen, J.-P. Deng, C.-Y. Mou, and F. J. García de Abajo, "Probing bright and dark surface-plasmon modes in individual and coupled noble metal nanoparticles using an electron beam," Nano Lett. **9** (1), 399 (2009).

[97] E. D. Palik, *Handbook of Optical Constants* (Academic Press, New York, 1984).

[98] J.-S. Huang, J. Kern, P. Geisler, P. Weinmann, M. Kamp, A. Forchel, P. Biagioni, and B. Hecht, "Mode imaging and selection in strongly coupled nanoantennas" Nano Lett. **10**, 2105 (2010).

[99] M. Liu, T.-W. Lee, S. K. Gray, P. Guyot-Sionnest, and M. Pelton, "Excitation of dark plasmons in metal nanoparticles by a localized emitter," Phys. Rev. Lett. **102**, 107401 (2009).

[100] W. Zhang, B. Gallinet, and O. J. F. Martin, "Symmetry and selection rules for localized surface plasmon resonances in nanostructures," Phys. Rev. B **81**, 233407 (2010).

[101] L. S. Slaughter, Y. Wu, B. A. Willingham, P. Nordlander, and S. Link, "Effects of symmetry breaking and conductive contact on the plasmon coupling in gold nanorod dimers," ACS Nano **4** (8), 4657 (2010).

[102] S.-C. Yang, H. Kobori, C.-L. He, M.-H. Lin, H.-Y. Chen, C. Li, M. Kanehara, T. Teranishi, and S. Gwo, "Plasmon hybridization in individual gold nanocrystal dimers: direct observation of bright and dark modes," Nano Lett. **10** (2), 632 (2010).

[103] R.-M. Ma, R. F. Oulton, V. J. Sorger, G. Bartal, and X. Zhang, "Room-temperature sub-diffraction-limited plasmon laser by total internal reflection," Nature Mater. **10**, 110 (2011).

[104] Q. Song, H. Cao, S. T. Ho, and G. S. Solomon, "Near-IR subwavelength microdisk lasers," Appl. Phys. Lett. **94**, 061109 (2009).

[105] K. Yu, A. Lakhani, and M. C. Wu, "Subwavelength metal-optic semiconductor nanopatch lasers," Opt. Express **18** (9), 8790 (2010).

[106] M. P. Nezhad, A. Simic, O. Bondarenko, B. Slutsky, A. Mizrahi, L. Feng, V. Lomakin, and Y. Fainman, "Room-temperature subwavelength metallo-dielectric lasers," Nature Photon. **4**, 395 (2010).

[107] S. L. Chuang, *Physics of Photonic Devices* (John Wiley & Sons, New York, 2009).

[108] K. J. Vahala, "Optical microcavities," Nature **24**, 839 (2003).

[109] A. W. Poon, F. Courvoisier, and R. K. Chang, "Multimode resonances in square-shaped optical microcavities," Opt. Lett. **26**, 632 (2001).

[110] S.-H. Kwon, J.-H. Kang, C. Seassal, S.-K. Kim, P. Regreny, Y.-H. Lee, C. M. Lieber, and H.-G. Park, "Subwavelength plasmonic lasing from a semiconductor nanodisk with silver nanopan cavity," Nano Lett. **10**, 3679 (2010).

[111] P. B. Johnson and R. W. Christy, "Optical constants of the noble metals," Phys. Rev. B **6**, 4370 (1972).

[112] E. Cubukcu, E. A. Kort, K. B. Crozier, and F. Capasso, "Plasmonic laser antenna," Appl. Phys. Lett. **89**, 093120 (2006).

AUTHOR'S BIOGRAPHY

Anil Kumar received his B. Tech. and M. Tech. degrees in Materials and Metallurgical Engineering from Indian Institute of Technology (IIT) Madras, Chennai, India in 2004. During this period he worked with Prof. T. Pradeep in the Department of Chemistry at IIT Madras on chemical synthesis of plasmonic nanoparticles and studied their effect on self-assembled monolayers. He was an undergraduate intern at I. Physikalisches Institut A, University of Aachen (RWTH) during summer terms of 2002-04 and another semester after completing his degree. His work at RWTH focused on instrumentation and characterization of sputter deposited thin films of transition metal oxides. He joined ECE at Illinois in January 2005 and has been working with Prof. Nicholas Fang since fall of 2006. He has worked on a wide range of projects involving thin films, microfabrication, optical characterization, and cathodoluminescence. His work has been published in *Nano Letters*, *Nanotechnology*, *Journal of Vacuum Science and Technology B*, *SPIE*, *EIPBN*, and *Material Research Society*.